A numerical investigation of wake recovery for an H- and X-shaped vertical-axis wind turbine with wake control strategies

Ajay, Adhyanth Giri; Ferreira, Carlos Simao

DOI
10.1063/5.0244810

Publication date
2024

Document Version
Final published version

Published in
Physics of Fluids

RESEARCH ARTICLE | DECEMBER 17 2024

A numerical investigation of wake recovery for an H- and X-shaped vertical-axis wind turbine with wake control strategies

Adhyanth Giri Ajay ; Carlos Simao Ferreira

Physics of Fluids 36, 127161 (2024)
https://doi.org/10.1063/5.0244810

Physics of Fluids ARTICLE pubs.aip.org/aip/pof

A numerical investigation of wake recovery for an H- and X-shaped vertical-axis wind turbine with wake control strategies

Cite as: Phys. Fluids **36**, 127161 (2024); doi: 10.1063/5.0244810
Submitted: 22 October 2024 · Accepted: 26 November 2024 ·
Published Online: 17 December 2024

View Online Export Citation CrossMark

Adhyanth Giri Ajay[a] and Carlos Simao Ferreira

AFFILIATIONS

Wind Energy, Flow Physics, and Technology, Faculty of Aerospace Engineering, Delft University of Technology, Delft 2629HS, The Netherlands

[a]Author to whom correspondence should be addressed: A.GiriAjay@tudelft.nl

ABSTRACT

Vertical-axis wind turbines (VAWTs), particularly in offshore wind farms, are gaining attention for their capacity to potentially enhance wake recovery and increase the power density of wind farms. Previous research on VAWT wake control strategies have demonstrated that the pitch offset is favorable for VAWT wake recovery. In the present study, an investigation on the wake recovery and its mechanisms for an H-Rotor and a novel X-Rotor VAWTs with fixed blade pitch offsets is conducted through qualitative and quantitative methods. The actuator line method is utilized in this study. Results indicate that the two rotors produce distinct vortex systems that drive the wake recovery process—which is augmented with pitch offsets. Through quantitative studies, the contribution of wake recovery due to advection increases dramatically with pitch offsets in the near wake. With pitch offsets, the inline available power increases up to 2.3 times for the rotors when compared to when there is no pitch offset. The mean kinetic energy flux occurs mostly above and below the rotors as well as the windward side, suggesting the mechanism of power replenishment for these rotors with pitch offsets. These results encourage further research into the effectiveness of wake recovery in the wind-farm level with the ground and atmospheric boundary layer influences.

I. INTRODUCTION

Offshore wind energy—considered one of the most sustainable energy resources—has been primarily dominated by horizontal-axis wind turbines (HAWTs) in the past several decades.[1] Vertical-axis wind turbines (VAWTs) have attracted significant attention as a promising addition to offshore wind energy due to their simpler blade design, lower cost, and their capability to operate in omnidirectional wind conditions.[2,3] Furthermore, the lower center of mass and overturning moments offered by VAWTs make them a valuable commodity for floating wind farms as well.[4]

In offshore wind farms, many turbines operate in the wake of other turbines. Therefore, the idea of wake recovery is essential to maximize the annual energy production of the offshore wind energy sector.[5,6] HAWTs have utilized various control strategies to manage and improve wake recovery. Techniques such as yawing[7–10] and tilting[11,12] can deflect the wake laterally or vertically, respectively. Recently, dynamic induction control methods like helix mixing have been studied and tested to enhance wake mixing and further increase wake recovery.[13,14]

VAWTs have been shown to potentially increase the power density of wind farms significantly[15–18] by varying the layout of the turbines. Numerical, experimental, and field investigations have shown that VAWTs can recover the wake much faster than HAWTs (considered as the recovery of 95% of freestream velocity)[19,20] without involving any control schemes. This phenomenon is predominantly ascribed to the heightened turbulent mixing within VAWT wakes, augmented secondarily by the lateral and vertical advection of wake attributed to the streamwise tip vortices.[21–23] However, the wake recovery in the near-wake region is primarily dominated by the advection of streamwise momentum.[24,25] Therefore, enhancing the advection in the near wake is paramount to increase the wake recovery downstream of the rotor.

As mentioned earlier, the advection of the wake in VAWTs is primarily driven by the streamwise tip vortices. From a purely aerodynamic perspective, redistributing the rotor loads of a VAWT creates stronger tip-vortices. Ferreira[26] first proposed that the rotor loads on VAWTs can be shifted either upwind or downwind by setting the blades at a fixed pitch offset. This was experimentally demonstrated by LeBlanc and Ferreira,[27,28] where the loads on the blades are increased in the upwind half and lowered in the downwind half when the leading edge of the blade is pitched toward the axis of rotation and vice versa. Two-dimensional (2D) numerical simulations by Jadeja[29] showed that the wake deflection increases significantly with a fixed blade pitch due to the stronger tip-vortices. Experiments later quantified the effect of blade pitching on the wake recovery process for a two-bladed H-shaped VAWT.[30,31] These experiments showed that there was a significant change in the lateral thrust of the rotor with blade pitching while slightly compromising the streamwise thrust. Huang[32] provided a Reynolds Averaged Navier–Stokes (RANS) based actuator line method (ALM) model validation study with lab-scale experiments. The validation was performed for a H-Rotor with a 0.3 m rotor diameter at the TU Delft Open Jet Facility, for which Particle image velocimetry (PIV) measurement planes are used to measure the flow at planes perpendicular to the streamwise direction, and the results showed good agreement between the experiments and the ALM model. In the same thesis, simulations for a full-scale 160 m diameter H-Rotor showcase the power loss associated with blade pitching for both isolated VAWTs and a 1 × 3 VAWT array. The study showed a maximum power loss of 12% for an isolated VAWT with 10° of blade pitch while obtaining roughly 300% increase in power (from a C_p of 0.09 to 0.38) for a downstream VAWT at 3 D downstream, where D is the diameter of the rotor.

Due to these advantages, newer designs of VAWTs are being developed to suit specific requirements. One innovative VAWT design is the X-Rotor,[33] which aims to reduce the levelized cost of energy (LCoE) of turbines (Fig. 1). This design departs from the traditional VAWT geometry by incorporating two sets of coned blades (upper and lower) arranged in an "X" shape (primary rotor) to extract kinetic energy from the wind and two small horizontal-axis wind turbines (secondary rotors) to generate electrical power mounted on the lower

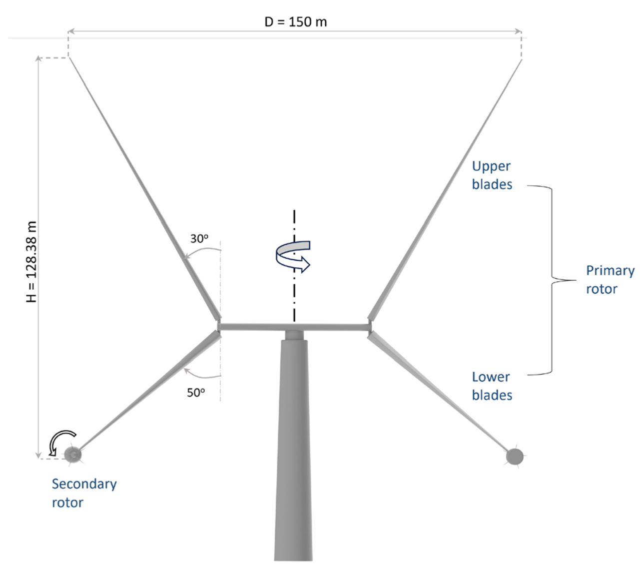

FIG. 1. A render of the X-Rotor turbine with geometrical dimensions from Leithead *et al.*[33] This figure is reused from Giri Ajay *et al.*[35]

blade tips. The turbine uses the concept of an "aerodynamic gearbox" where the angular velocity of the primary rotor enhances the incident wind speed of the secondary rotor. This allows conventional gearboxes to be connected directly to the secondary rotors, without requiring gearboxes, which reduces the weight of the design and mitigates extra operational and maintenance costs. The primary rotor features pitch-controlled upper blades, which are engineered to shed aerodynamic power in above-rated wind conditions. The lower blades are not pitch-controlled.

As a novel VAWT concept, the X-Rotor's wake and wake recovery studies are still in the early stages. However, recent experimental research on a scaled version of the primary rotor has provided insights into the rotor loading and the three-dimensional aerodynamics within its volume.[34] This study found that the coned blades create significant three-dimensional effects, with the shed vorticity forming highly elliptical shapes downstream, unlike that of the H-Rotor. Additionally, a numerical investigation of the full-scale primary rotor indicated that using fixed pitch offsets in the X-Rotor significantly alters the vertical induction within the rotor volume,[35] resulting in a 5%–8% power loss at pitch angles of 5° and −5° and a significant 15%–22% power loss at pitch angles of 10° and −10°. Furthermore, an experimental study of the X-Rotor with fixed pitch offsets of the upper blade showcases the wake-deflection capabilities.[36] Nonetheless, there remains a lack of understanding about the vortex system of this rotor at far-wake locations and its behavior under various fixed pitch offsets. Additionally, there is a lack of information on how this vortex system differs from the standard H-Rotor geometry and how this affects the wake recovery capabilities. Bensason *et al.*[36] attempted at showing this difference experimentally but could not capture the full frontal area of the X-Rotor to systematically compare the differences between the rotor types.

The present work is a direct expansion of our previous conference publication (Giri Ajay and Simao Ferreira[37]), which focused on understanding the impact of rotor geometry on wake recovery quantification. There, we compared and quantified the wake between the X-Rotor and an H-Rotor to the X-Rotor at different fixed pitch offsets. In that paper, we concluded that other than the tip-vortices, the X-Rotor experienced a significantly large root vortex, which hindered the wake deflection capabilities of the rotor, as the wake in the lower half was not advected due to the weak lower tip-vortices. The root vortex appears due to the difference in circulation between the upper and lower blades at fixed pitch offsets—as only the upper blades are pitched. Additionally, instead of using a characteristic length scale to analyze the wake downstream, we used their corresponding rotor diameters, which does not account for wake similarity. Therefore, the aim of this study is twofold: (1) to understand the parameters that drive the wake recovery mechanism behind the H-Rotor and X-Rotor and (2) to analyze the wake recovery capability of the H-Rotor and the X-Rotor through a fair qualitative and quantitative approaches. Here, the former is our primary objective, while the latter is a secondary objective that facilitates the former. To facilitate (2), we deviate slightly from the operating design of the X-Rotor and allow pitch control for the lower blades along with the upper blades—which is elaborated more in Sec. II.

II. METHODOLOGY

This section discusses the models used in this work (Sec. II A), the scaling used for the H-Rotor geometry (Sec. II B), and define the wake length scale used in the analysis (Sec. II C). Finally, we highlight the geometry and setup used in this study (Sec. II D).

A. Actuator line model

The actuator line method (ALM) implementation, first proposed by Sørensen and Shen,[38] is a blade element formulation that represents wind turbine blades as discretized blade line elements that each, in turn, represent a 2D airfoil profile. The static airfoil lift and drag data are input through airfoil polars or lookup tables. The forces produced are projected onto the fluid domain as source terms in the momentum equations through the means of a spherical Gaussian regularization kernel, η [Eq. (1)]. This η is required to avoid the singularity from the vortex formed for each line element, which would otherwise induce instability in the finite volume cells

$$\eta(r) = \frac{1}{\varepsilon^3 \pi^{3/2}} \exp\left[-(r/\varepsilon)^2\right], \tag{1}$$

where ε is the parameter that adjusts the width of this function and r is the distance between the cell and the line element.

The implementation we used here in this study is the *turbinesFoam* library[39] to be used in *OpenFOAM*-v2106.[40] In ALM models, the thrust T and the blade loading are preserved through the parameter $\varepsilon/\Delta_{grid}$, where Δ_{grid} is the local grid length.[38] *turbinesFoam* follows the suggestion of Troldborg[41] to choose $\varepsilon/\Delta_{grid} = 2$. However, later works of Martínez *et al.*[42] and Jha *et al.*[43,44] show that varying this parameter shows a significant change in blade loads and power estimations of the rotor. Therefore, we tuned $\varepsilon/\Delta_{grid}$ by performing a sensitivity study of the normal load profile as a function of $\varepsilon/\Delta_{grid}$. The normal loads are compared with a free-wake vortex model—CACTUS[45] that was previously verified against blade-resolved Unsteady Reynolds-Averaged Navier–Stokes (URANS) Computational fluid dynamics (CFD) models for the X-Rotor at different operating conditions.[35] In addition to this tuning, *turbinesFoam* does not currently account for coned blades. Therefore, we modified the source code to account for the coned blade angles.[46] Detailed information about these modifications as well as a sensitivity study is presented in Appendix A to not dilute the main findings of our study. Overall, we chose $\varepsilon/\Delta_{grid} = 5$ for our implementation of the H-Rotor and $\varepsilon/\Delta_{grid} = 2$ for the X-Rotor for $\Delta_{grid} = D/40$. These values are constant along the span as the mesh resolution is also constant.

In this study, the flow is treated as incompressible, homogeneous, and Newtonian with a density of $\rho = 1.225\,\mathrm{kg\ m^{-3}}$ and a kinematic viscosity of $\nu = 1.5\,\mathrm{m\ s^{-2}}$. As mentioned earlier, we use the Unsteady Reynolds-Averaged Navier–Stokes (URANS) equations in the *pimpleFoam* solver in this study to capture the time-resolved wake. Furthermore, we implement the use of the $k-\varepsilon$ turbulence closure model.[47] We chose this closure model than other popular approaches like the $k-\omega$ SST model[48] as we do not have a physical rotor that requires capturing the separation. Moreover, $k-\varepsilon$ has been documented in VAWT simulations to show good prediction at higher tip-speed ratios ($\lambda \geq 3$).[49] The inflow velocity U is kept at a constant $12\,\mathrm{m\ s^{-1}}$ with a low turbulence intensity TI of 0.22%.

The simulation domain ranges from $-5\,D$ upwind to $15\,D$ downwind, where D is the rotor diameter corresponding to the simulation. This is in accordance with the suggestions from Rezaeiha *et al.*[50]. It extends laterally from $-4\,D$ to $4\,D$ and vertically from $-3.5\,D$ to $3.5\,D$. For this domain, a fine mesh region of resolution $D/40$ extends from $-1\,D$ to $7\,D$, enveloping up to $1\,D$ on either lateral and vertical directions from the rotor center. This region is encompassed in a coarser mesh region of $D/20$ resolution ranging from $-1.5\,D$ to $11\,D$ up to $1.5\,D$ either side laterally and vertically. The sides, top, and bottom edges of the domain are zero gradient, while the outlet is treated as an inlet–outlet boundary.

B. Scaling the H-rotor

To compare the wake recovery capabilities between two different rotors, we choose key parameters that govern the geometry scaling and the thrust scaling of the rotor—the frontal area A, the aspect ratio AR, the tip-speed ratio λ, and the thrust coefficient C_T. The H-Rotor is designed to match these parameters to that of the X-Rotor for this study. The geometry of the X-Rotor is provided in Leithead *et al.*[33] and Giri Ajay *et al.*[35] Using this, the diameter D and height H can be obtained. However, to obtain the chord c, we need to match T and λ. The CACTUS model is once again employed here for the purpose of scaling the H-Rotor. This model is also previously tested for H-Rotor geometries,[51] with caveats about using it primarily for high λ (≥ 4) and small angles of attacks α (ideally below the static stall angle of airfoils). Therefore, for $\lambda = 4$, we identified the solidity of the H-Rotor ($\sigma_H = Nc_H/D$) required to match the thrust of the X-Rotor (Fig. 2), where N is the number of blades, c_H is the chord of the H-Rotor, and D is the diameter of the rotor.

C. Characteristic length scale for the wake similarity

Both the H-Rotor and the X-Rotor are scaled to have the same thrust T, frontal area A, and aspect ratio AR. However, the diameter D of each rotor is significantly different from each other. Therefore, to maintain the similarity in the analysis of wake of these rotors, a characteristic length scale L is used to represent the distance downstream at which the wake of the two rotors attains similarity. We implement a modified concept of the "momentum length scale" to normalize all the length scales in the streamwise direction based on the implementation

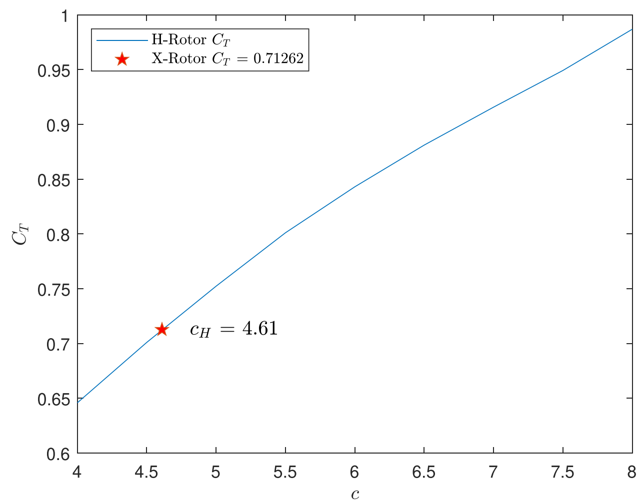

FIG. 2. Thrust coefficient C_T as a function of chord c for the H-Rotor for the tip-speed ratio $\lambda = 4$. The red start indicates the C_T of the X-Rotor also at $\lambda = 4$, from Giri Ajay *et al.*[35]

by Meunier and Spedding.[52] This implementation was later demonstrated by Shamsoddin and Porté-Agel[53] to work well for VAWTs. We modify this characteristic length scale from $L = \sqrt{(4/\pi)A}$ to $L = \sqrt{A}$, which we believe is an acceptable level of simplification considering that our wake shapes with the pitch offsets would not converge to a disk-like shape, as documented by Huang *et al.*[30]

D. Test geometry and setup

After applying the scaling and identifying the solidity of the H-Rotor, both rotor dimensions and operational conditions with scaling information are provided in Table I.

A is the frontal area, σ represents the solidity, and AR is the rotor aspect ratio. U is the homogeneous freestream velocity, and the tip-speed ratio is given by λ. σ for the X-Rotor is evaluated as $\sigma_X = N \sum c_i \Delta H_i / A$, where ΔH_i is the difference in height between blade sections, and c_i is the mean local chord of the blade section. This is done due to the coned blades of the X-Rotor. On top of the coned blades, the X-Rotor's upper and lower blades are tapered with different airfoil sections from the root to the tip. The upper blade root is made up of a NACA0025 section with $c = 10$ m, while the lower blade root section is the same section but with $c = 14$ m. The detailed geometry of the X-Rotor is described by Giri Ajay *et al.*[35]

NACA0021 polars at chord Reynolds number $Re = 1.5 \times 10^7$ are generated using XFOIL and are used for the H-Rotor turbine. The X-Rotor has a constant Re value of 1.5×10^7 (constant product of relative speed and local chord) at each blade section along its span. The polars used here are from the verified data set presented in Giri Ajay *et al.*[35]

The secondary rotors are not included in the simulation of the primary rotor to enable a more direct comparison in the rotor scale.

TABLE I. Geometry and operating conditions of the two rotor configurations.

Rotor type	D (m)	AR	σ	A (m^2)	U (m s^{-1})	λ
X-Rotor	150.00	0.857	0.17	12 870	12	4
H-Rotor	122.55	0.857	0.05	12 870	12	4

The tower is ignored in both rotor configurations to include only the lift-producing surfaces.

Three different pitch offsets ($-10°$, $0°$, and $+10°$) of the blade are considered for each turbine as shown in Fig. 3. The positive pitch indicates the leading edge pointing toward the rotation axis, while the negative pitch is associated when the leading edge points away from it. Both the rotors have a counterclockwise rotation to be positive, and the azimuth $\theta = 0°$ is considered to be where the leading edge is against freestream with the chord parallel to it.

No dynamic stall models are used in this study as tuning the coefficients of the Leishman–Beddoes dynamic stall model would be different for both rotors. Neglecting the dynamic stall can impact the regions close to the root with positive and negative pitch angles, which might reduce any differences observed between the rotors slightly. Additionally, flow curvature models are also ignored as it would be difficult to predict its impact on the coned blades of the X-Rotor. The simulations are computed over a flow simulation time of 300 s, which corresponds to about 30 revolutions for the X-Rotor and 37 revolutions for the H-Rotor. The simulations [computed on Delft High Performance Computing Center (DHPC)[54] with 48-core Intel XEON E5-6248R 24C 3.0 GHz] took in total about 336 CPU hours for each case.

III. RESULTS AND DISCUSSION

This sections highlights the rotor level performance and load assessment (Sec. III A), discusses the vorticity and velocity fields of the two rotors (Sec. III B), quantifies the wake displacement (Sec. III C), and evaluates and discusses the available power behind the two rotors (Sec. III D). To give further insight into the mechanism of the wake recovery, we present a discussion on the momentum recovery contributions (Sec. III E) and into the mean kinetic energy flux (Sec. III F).

A. Rotor performance and load assessment

The distribution of normal load as a function of the pitch angle is given in Fig. 4 for both H- (solid lines) and X- rotors (dashed lines). The loads are post processed based on the local information of the inflow velocity, angles of attack, and the airfoil polars. We can observe that the loads are more evenly balanced between the upwind (UW and UL) and the downwind halves (DW and DL) at $\beta = 0°$, with slightly

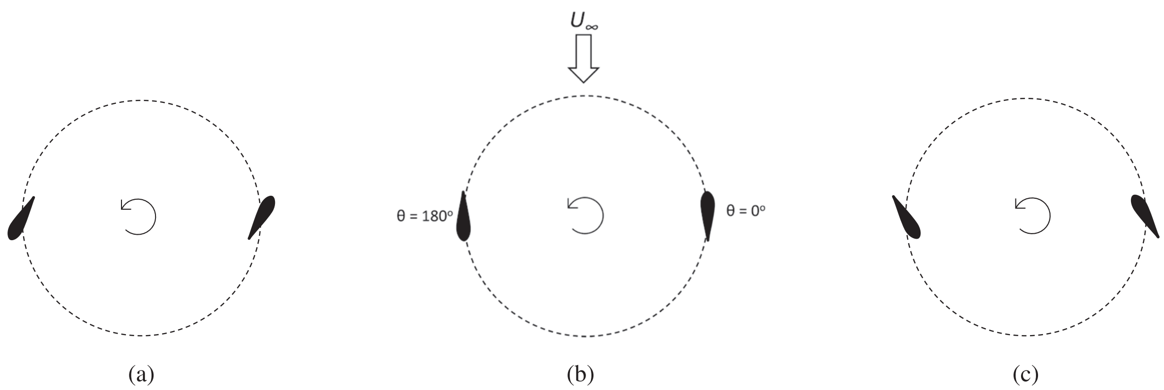

FIG. 3. Top view of the upper blade tip with (a) negative, (b) zero, and (c) positive pitch offsets. θ indicates the azimuth and U_∞ is the freestream velocity. This figure is reused from Giri Ajay *et al.*[35]

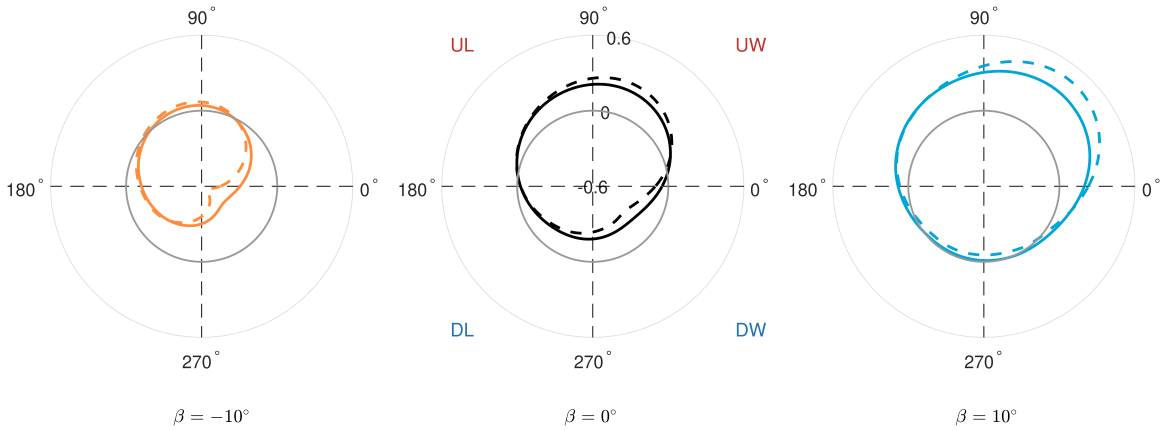

FIG. 4. A polar plot of the normal loads of the H-Rotor (solid line) and X-Rotor (dashed line) at blade pitch offsets $\beta = [-10°, 0°, 10°]$, from left to right, respectively. The loads are normalized by the surface area of each corresponding rotor. The solid gray circle indicates a null normal load, i.e., the loads are positive outside the circle and negative inside it. The center of the plot indicates a load of −0.6, while the circumference of the plot indicates a load of 0.6. The quadrants of the azimuth are marked as upwind-windward (UW), upwind-leeward (UL), downwind-leeward (DL), and downwind-windward (DW). The freestream is from the top along the 90° line.

higher amplitudes in the downwind half. This is contrary to the previously extensive documentation of VAWT blade loads;[32,35,36] however, this odd behavior is due to the lack of the flow curvature model. With the flow curvature model, the blade would experience a small increase in the inflow angle, which would result in a more upwind dominated load distribution at this pitch offset. Furthermore, we can see that the loads favor the windward direction (UW and DW). Therefore, we can expect the windward vortices to be more dominant in the system. We also notice that the X-Rotor loads are slightly higher than those of the H-rotor in the windward side. This means that the vorticity strengths of the X-Rotor would be higher.

At $\beta = -10°$, we can see that the upwind loads are severely reduced and the highest loads are in the DW region. Based on the experimental documentation by Huang *et al.*[30] and Bensason *et al.*,[36] the vortices originating from the DW region are the most dominant in the vorticity system. This is also indicative that most of the wake is produced by the downwind half, as it contributes most to the thrust of the rotor.

At $\beta = 10°$, the loads redistribute to be dominant in the upwind region, with the peak magnitude at UW. Contrary to the previous configuration, this means the vorticity system is dominated by the UW vortices. Therefore, the wake is mostly generated by the upwind half, and little variation in the wake can be expected as the flow passes through the downwind half as the loads are small. The implications of these loads on the vortex system and the wake are presented later in Sec. III B, along with a detailed discussion about the vortex systems themselves.

TABLE II. The coefficient of streamwise C_{Tx} and lateral thrust C_{Ty} for both the H- and the X-Rotors at blade pitch angles $\beta = [-10°, 0°, 10°]$.

	C_{Tx}			C_{Ty}		
Pitch β	−10°	0°	10°	−10°	0°	10°
H-Rotor	0.56	0.65	0.55	−0.37	−0.03	0.28
X-Rotor	0.53	0.64	0.56	−0.52	−0.08	0.33

With the redistribution of loads, the thrust in the streamwise and lateral directions also changes. Table II presents the corresponding thrust in the streamwise C_{Tx} and lateral C_{Ty} direction, with the introduction of blade pitch angles. We did not consider the power performance of the two rotors in these cases, as we cannot draw meaningful conclusions due to the discrepancies between the tangential loads and the CACTUS model, as seen in Appendix A. First, the streamwise thrust for both the rotors is quite similar, indicating that the scaling continues to be relevant, but the magnitudes are much lower than the design value of 0.71 as shown in Fig. 2. This discrepancy is due to the way blade loads are projected in the fluid domain, which is further elaborated in Appendix A. We can see that for both the rotors, as the loads are redistributed to be DW dominant ($\beta = -10°$), the streamwise thrust reduces from the baseline case but the lateral thrust magnitude increases significantly. Interestingly, the X-Rotor shows much higher lateral thrust values compared to the H-Rotor. This will be elaborated further while understanding the vortex system of the rotor. The converse is true when the loads are redistributed to be UW dominant ($\beta = 10°$), and the lateral thrust is now in the opposite direction.

B. Vortex system and corresponding velocity fields

To better understand the physics of the wake deformation, the vortex system produced by the two rotors will be addressed first. The time-averaged streamwise vorticity isometric contours ($\overline{\omega}_x D/U_\infty$) for the three pitch cases of both the rotors of $\beta = -10°, 0°, 10°$ at several downstream locations ($X/L = 1, 3, 5, 7,$ and 9) are presented in Fig. 5. The windward side of the rotor is represented as $Y/D > 0$, and the leeward side is $Y/D < 0$. The rotor is centered at X, Y, Z = 0. For the H-Rotor, Z = 0 is equidistant between its two struts, while for the X-Rotor, it is the root section of the X-Rotor where the upper and lower blades meet. The dominant vortices are marked as $R_{a,b}$, where R refers to the rotor type (H- or the X-Rotor), and subscript a depicts the lateral location of the vortex (windward/leeward) and b denotes its vertical location (top, root, bottom).

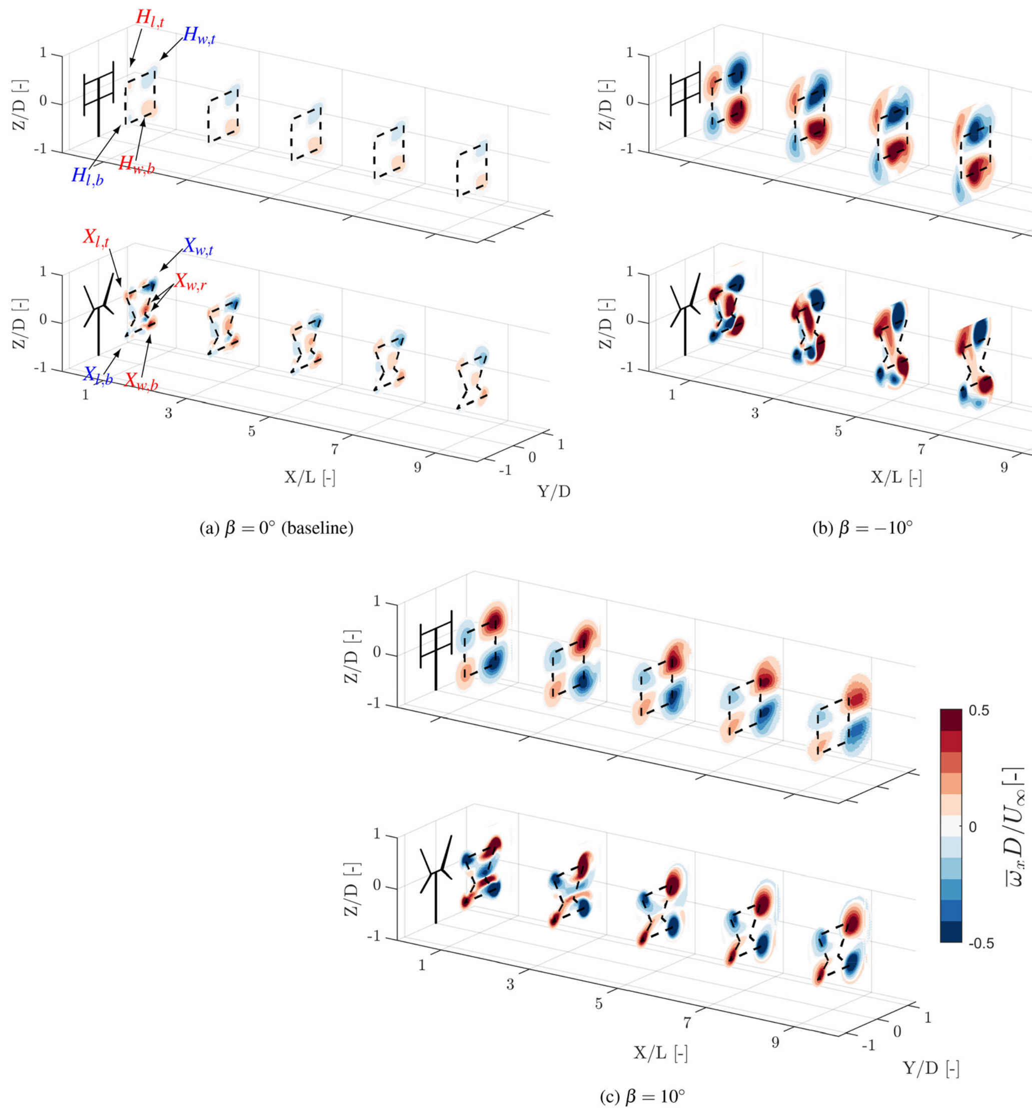

FIG. 5. Normalized streamwise vorticity $\overline{\omega}_x D/U_\infty$ contours of the H-Rotor and X-Rotor with the pitch offset $\beta = -10°, 0°, 10°$, respectively, at downstream locations $X/L = 1$, 3, 5, 7, and 9, where L is the characteristic streamwise length scale. The black dashed lines indicate the projected frontal area of the rotor on the corresponding plane. The lateral Y and the vertical Z spatial coordinates are normalized by the diameters D of each rotor, respectively. The labeled vortices follow the rubric $R_{a,b}$, where R corresponds to the rotor type (H or X), subscript a indicates the lateral location of the vortex (windward or leeward), while b depicts the vertical location of the vortex (top, bottom, or root). Counter-clockwise is considered positive viewed from downwind and vice versa.

The $\beta = 0°$ provides a baseline of the vortex system without any pitch offset. In the H-Rotor, we observe blade tip-vortices in both the windward and leeward sides, with the former much stronger than the latter, which is discussed in Sec. III A. The leeward vortices ($H_{l,t}$ and $H_{l,b}$) continue to remain insignificant to the vortex system as they lose energy due to turbulent dissipation beyond the near wake region ($X/L = 1$). This is correlated with the variation of the turbulence intensity I in Appendix C. Meanwhile, the windward vortices stay relevant throughout the domain. In the X-Rotor, we observe higher vortex strengths. Otherwise, the X-Rotor vortex system exhibits similar behavior except for the addition of the root vortices $X_{w,r}$ and $X_{w,b}$. These vortices, as previously documented by Giri Ajay and Simao Ferreira,[37] arise from the difference in circulation between the upper and lower blades. Moreover, it moves vertically up and leeward as the wake propagates downwind due to the induced velocity field from $X_{w,t}$ and $X_{w,b}$. However, in this instance, we see two in the windward side and fainter pairs in the leeward side. They are the root vortices from the upper blade (red) and lower blade (blue)—as we see that the former is stronger in magnitude as the latter dissipates earlier. These root vortices will play an important role in the wake advection in the cases with pitch offset.

At $\beta = -10°$, the downwind vortices dominate the vortex system even more, as previously discussed in Sec. III A. In both the rotors, the magnitude of all the vortices are significantly higher than the baseline $\beta = 0^\circ$ case, with the windward vortices remaining stronger than the leeward ones. For the H-Rotor, in the near wake, both $H_{w,t}$ and $H_{w,b}$ cores can be observed to propagate leeward, due to their mutually symmetric induced velocity field. At further downstream locations, the leeward vortices influence this propagation by forcing them to move vertically away from the frontal area of the rotor. However, due to the difference in vortex strengths between the leeward and windward vortices, the leeward vortices tend to swirl around the stronger windward vortices, which is noticeable after $X/L = 7$. At far downstream locations, the dissipation of the vortex is more apparent and the vortices appear to be stagnated. In the X-Rotor, $X_{w,t}$ and $X_{w,b}$ are not symmetric, due to the presence of $X_{w,r}$, which causes them to propagate at different rates in the leeward direction. Meanwhile, $X_{w,r}$ is quite weak compared to the other vortices, as it can be seen dissipating earlier than the other vortices. This is in stark contrast with our previous findings in Giri Ajay and Simao Ferreira.[37] This is attributed to the upper and lower blades pitched equally in this study, which does not increase the circulation difference from the baseline case. Additionally, $X_{w,r}$ is propelled vertically by the other vortices as the flow moves downstream. However, we also notice both the $X_{w,r}$ increasing in magnitude with this pitch offset, further indicating that these two windward root vortices originate from the upper (red) and lower (blue) blades. These vortices are much stronger than the baseline case, allowing rapid advection freestream from the windward side into the rotor area. This explains the lateral thrust (Table II) being much higher than the H-Rotor. This affects the leeward movements of $X_{w,t}$ and $X_{w,b}$ and instead shows signs of moving vertically out of the frontal area of the rotor. As a result, at $X/L = 7$, $X_{w,t}$ is outside of the rotor frontal area in contrast to $X_{w,b}$. Additionally, the root vortex appears to coalesce with $X_{l,t}$ and together swirl around the windward tip-vortices beyond $X/L = 7$. Regardless, the $X_{w,t}$ and $X_{w,b}$ still remain significant in the system, which should bring in freestream from the windward side into the frontal area of the rotor.

With the loads redistributed to the front in the $\beta = 10^\circ$ case, the vortices produced in the upwind half dominate the system. This is accurate to the discussion in Sec. III A. This is shown by the change in the direction of the vortices from the $\beta = -10^\circ$ case. In the H-Rotor, $H_{w,t}$ and $H_{w,b}$ are mutually propelled toward the leeward side due to their induced velocities, while $H_{l,t}$ and $H_{l,b}$ appear to be stationary. This is due to the induced velocity from the windward vortices being considerably stronger than the leeward vortices, which negates the induced velocities from the leeward vortices for their lateral movement. At further downwind locations, $H_{w,t}$ and $H_{w,b}$ continue to mutually propel themselves leeward away from the frontal area of the rotor (approximately $1\,D$ leeward at $X/L = 7$) while simultaneously pulling the leeward vortices toward them. However, this is not quite significant as the vortices dissipate earlier due to the turbulence and have less impact on the flowfield. In the X-Rotor, the root vortices $X_{w,r}$ are observed again to be stronger and opposite to the baseline case but at a much lower strength than all the other vortices in the system. Additionally, they are also much weaker than the $\beta = -10^\circ$ case, which makes the lateral thrust of this case align well with the H-Rotor. However, this affects the windward vortices from being mutually propelled as $X_{w,r}$ influences $X_{w,t}$ and $X_{w,b}$ that opposes their movement. $X_{w,r}$ gets pulled by the windward tip-vortices in the near wake and dissipates sharply after $X/L = 3$. Toward $X/L = 5$ and further downstream, the root vortices swirl around the windward tip-vortices; however, it does not appear to affect the vortices significantly. The leeward vortices $X_{l,t}$ and $X_{l,b}$ also do not show signs of mutual propulsion due to the negation of induced velocity, as observed in the H-Rotor as well.

The time-averaged streamwise velocity fields (u/U_∞) corresponding to the vortex system are shown in Fig. 6, where the dashed black lines trace the frontal area of the two rotor types. Values of u/U_∞ of unity and above have been removed from the plot for clarity of the wake shape.

The $\beta = 0^\circ$ serves as a benchmark to observe the wake shape without pitch modification. In the H-Rotor, the wake overall expands laterally and vertically outwards, driven by the tip-vortices. Due to the streamtube expansion, the velocity deficit in the wake increases until about $X/L = 3$, beyond which the deficit decreases due to the advection and turbulence. Due to the presence of the windward tip-vortices, the wake shape continues to be pushed vertically, until about $X/L = 5$ from which the vortices dissipate and the advection of the wake becomes less significant. Similar behavior of the streamtube expansion as well as the vertical expansion is observed in the X-Rotor. However, there is a noticeably higher velocity deficit in the upper half of the rotor area, while the lower half has a lower velocity deficit than the H-Rotor. In the X-Rotor, the upper blades produce much larger loads than the lower half, which causes the thrust to be not symmetric between the top and bottom.[35] As the thrust is the same for both the rotors, the upper half produces a larger velocity deficit to compensate for the lower half. Interestingly, the wake appears to recover faster than the H-Rotor, as at $X/L = 5$, the region with high velocity deficits in the X-Rotor are smaller than in the H-Rotor. This is attributed to higher turbulent contribution to the wake recovery, which is elucidated in Sec. III E and in Appendix C.

At $\beta = -10^\circ$, there is an increased vertical expansion with large lateral contraction on the windward side for both rotors, which results in the wake being stretched vertically—much more than the baseline case. This is driven by the stronger tip-vortices that result in the leeward-vertical advection of the wake. In the H-Rotor, the two dominant windward vortices push the wake vertically out and bring freestream laterally into the frontal area of the rotor. It can be seen that at $X/L = 7$, almost all of the flow in the frontal area of the rotor is 90% U_∞ and above, indicating good wake recovery compared to the baseline case. At $X/L = 7$ and beyond, due to the swirling of the leeward vortex with the windward vortex, the wake is observed to enter back into the frontal area of the rotor from the top and the bottom. For the X-Rotor, because of the asymmetric geometry as well as due to the root vortex $X_{w,r}$ moving vertically toward the $X_{l,t}$ and $X_{l,b}$, the wake in the top-half of the rotor ejects vertically out of the frontal area rapidly, while the bottom vortices mutually push the wake below. This is clearer at $X/L = 5$, where most of the wake is displaced above the rotor, while only a small portion is displaced below the rotor. Moreover, due to the coned geometry of this rotor, the wake at $X/L = 7$ still remains inside the frontal area of the rotor in contrast with the H-Rotor where the wake is mostly outside. Similar to the H-Rotor, the wake of the X-Rotor at far downstream locations does shows signs of reentering the frontal area of the rotor. However, the velocity deficits are much smaller due to the increased turbulence (Appendix C). This is reflected in the available power of the rotor, which is discussed in Sec. III D.

In comparison, at $\beta = 10^\circ$, the wake shape looks considerably different due to an increased lateral expansion accompanied by the

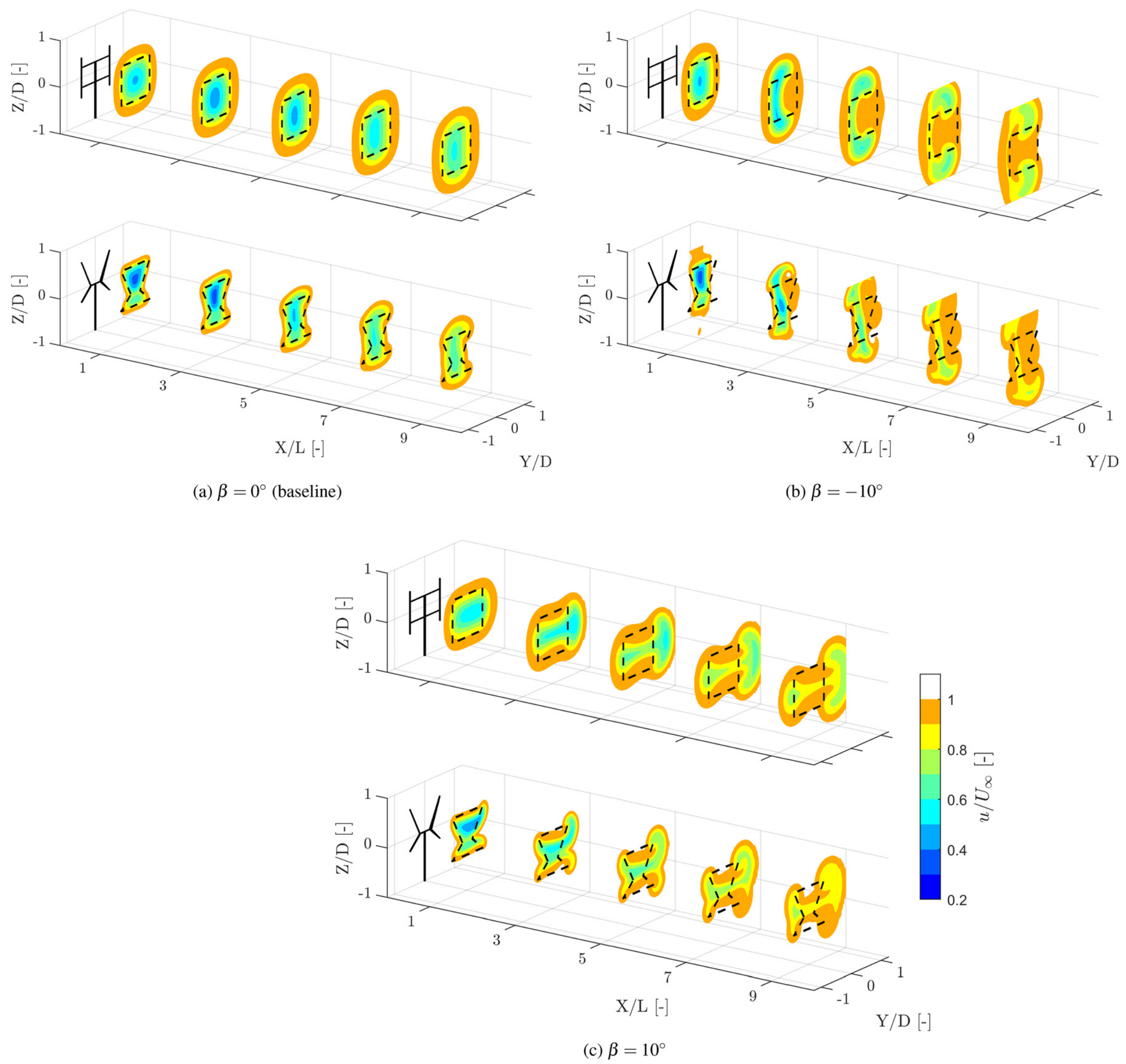

FIG. 6. Normalized streamwise velocity (u/U_∞) contours of the H-Rotor and X-Rotor with pitch offset $\beta = -10°, 0°, 10°$, respectively, at downstream locations $X/L = 1$, 3, 5, 7, and 9, where L is the characteristic streamwise length scale. The black dashed lines indicate the projected frontal area of the rotor on the corresponding plane. The lateral Y and the vertical Z spatial coordinates are normalized by the diameters D of each rotor, respectively. Values of freestream and above are hidden to enhance the visibility of the wake in this isometric perspective.

vertical contraction of the wake. This is observed at all downstream locations for both the rotors. In the H-Rotor, the two dominant windward tip-vortices working together eject a majority of the wake laterally by inducing a large lateral velocity component in the flow. This brings freestream to the frontal area of the rotor from the top and bottom due to the induced vertical velocity component. Similar to the $\beta = -10°$ case, the wake recovery is much faster in this pitch offset compared to the baseline case. At $X/L = 7$, a large portion of the wake is outside of the frontal area, with the wake squeezed by the high momentum flow entering the rotor from the top and bottom. In the X-Rotor, as the $X_{w,t}$ is stronger than $X_{w,b}$, most of the wake is laterally ejected by the former as the wake also moves vertically up outside the rotor area. The leeward vortices also eject the wake out in the leeward direction but is not as significant as the windward vortices. This pattern is also observed at planes further downstream. However, the velocity deficit inside the frontal area of the X-Rotor is significantly lower compared to the baseline case, which align with the results observed by Huang, Sciacchitano, and Ferreira[30] where the pitch offsets from the blades significantly aid the wake recovery process compared to the cases without any blade pitch offsets. Visually, it can be seen that the advection process subsides around $X/L = 7$, where the wake is recovered primarily due to the turbulence in the flow. In both these rotors, we can see the wake is not completely outside the rotor area, in contrast to the far wake of $\beta = -10°$. In this study, this difference is because the $\beta = -10°$ amplifies the vortex strengths from the baseline case, while the $\beta = 10°$ inverts the vortices—which is not as effective. The quantification of advection in these configurations can be clearly visualized in Sec. III E.

The next set of analyses entail the quantification of the wake recovery, as well as providing insight into the mechanisms that drive the wake recovery process at each location in the streamwise direction.

C. Wake displacement

To quantify the wake deflection due to advection, methods that characterize the wake shape are required based on the pitch angles for control strategies. The wake center deflection is a common analysis method to characterize the wake center of HAWTs using either a Gaussian shape fitting algorithm[55,56] or a "center of mass" approach for HAWTs[9,30,57,58] and VAWTs.[30,59] Due to the pitched blades, the wake no longer fits the Gaussian shape. Therefore, in this study, we use the "center of mass" approach. This approach was initially used to characterize HAWT, where the wake shape is defined by a pair of counter-rotating vortices when the rotor is yawed or tilted. However, VAWTs such as the H- and the X-Rotor have multiple such pairs (top and bottom tip-vortices for the H- and additional root vortex pairs for X-Rotor), which leads to the wakes moving in both the windward and leeward directions. Therefore, the existing "center of mass" method would not truly quantify the wake deflection, as there are several instances in VAWTs where these results can be misleading. For instance, in an idealized turbine where the vortices between the windward and leeward directions would be equal strength, with pitch offsets, the wake would move equally in both the windward and leeward directions—thus resulting in a null wake center displacement as the system becomes symmetric along the vertical-axis. While this is not true for a more realistic turbine, the results would nonetheless be a misrepresentation of the true wake advection capabilities of the turbine.

Therefore, for this study, we modify the existing "center of mass" method to not provide the wake center deflection, but rather a wake displacement—a quantification of the shift in wake from middle of the rotor. In this method, the wake center shifts in the lateral $y_c(X)$ and vertical $z_c(X)$ directions are represented as

$$y_c(X) = \frac{\int\int |y|\, \Delta U(x,y,z)\, dy\, dz}{\int\int \Delta U(x,y,z)\, dy\, dz}, \quad \text{and}$$
$$z_c(X) = \frac{\int\int |z|\, \Delta U(x,y,z)\, dy\, dz}{\int\int \Delta U(x,y,z)\, dy\, dz}, \tag{2}$$

where $|y|$ and $|z|$ would be the absolute of the spatial data, $\Delta U(x,y,z) = U_\infty - \overline{u}(x,y,z)$, $\overline{u}$ is the time-averaged velocity, and U_∞ is the free-stream velocity, and the discrete surface integration is done over the spatial data.

With the absolute values of spatial information, the integral of the leeward and windward wakes would no longer oppose each other. Instead, the result would depict the average shift of the wake center in a given direction, which would be more meaningful and representative of the wake deflection in opposing directions with pitch offsets. This approach, which is used in the analysis of this study, compromises the physical significance of the wake center in favor of better representing the wake deflection as a whole. To understand the physical wake center deflection, a brief analysis based on the traditional approach is discussed in Appendix B. The results and discussions from the traditional approach give insight into how the traditional quantification cannot be a good representation of wake deflection for VAWTs with blade pitch offsets.

The wake displacement in the lateral y_c and vertical z_c for the H- and the X-Rotors at pitch offsets $\beta = -10°, 0°, 10°$ is presented in Fig. 7 for downstream locations $X/L = [0, 10]$ for both rotors.

In all cases, the wake displacement at $X/L = 0$ is not zero, unlike HAWTs. This is because the plane only captures the wake of the upwind half, with the wake displacements corresponding to the loads, as previously seen in Fig. 4. The planes downstream of the rotor include the wake of the downwind half, which shifts the wake more to the center. This results in a much larger wake displacement at $X/L = 0$, while subsequently reducing at $X/L = 1$.

At $\beta = 0°$, both the rotors show lateral and vertical wake displacements. This is expected as we are no longer analyzing wake deflection but rather a shift from the middle of the rotor. However, the y_c/D remains consistently in the same range. This quantifies the lateral contraction of the rotor while showing gradual vertical expansion elucidated by the steady increase in z_c/D for both rotors.

At $\beta = -10°$, the wake is ejected vertically out, without much lateral movement. This is observed by the large z_c/D throughout the domain and low y_c/D. The y_c/D for both the rotors are, in the near wake, higher than their corresponding values in the baseline case. This is because of the heightened lateral contraction due to the larger windward vortices in the near wake, beyond which most of the wake is driven up and down by the upper and lower vortex pairs, respectively. Moreover, beyond $X/L = 4$, the opposite occurs. As the wakes are ejected out of the rotor area, the windward vortex pulls them, this resulting in the slight windward movement of the wake regions with

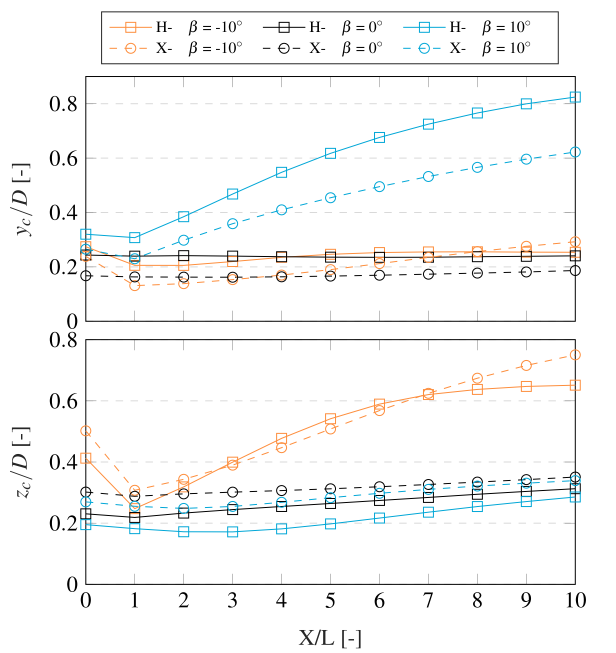

FIG. 7. The wake displacement in the lateral (y_c/D) and vertical (z_c/D) directions. Solid lines with squares represent the H-Rotor, and dashed lines with circles represent the X-Rotor. Orange, black, and cyan indicate pitch offsets of $\beta = -10°, 0°, 10°$, respectively.

large velocity deficits. This effect artificially increases y_c/D in these downstream planes. Interestingly, the z_c/D of the H-Rotor becomes asymptotic after $X/L = 7$ in contrast to that of the X-Rotor. This is attributed to the swirling effect discussed in Fig. 5, which reduces the vertical advection of the wake. The X-Rotor shows the largest z_c/D before $X/L = 3$ and beyond $X/L = 7$. The latter is due to the aforementioned swirling of the H-Rotor's windward vortices. The former is due to the uneven load distribution between the upper and lower halves of the X-Rotor. The upper half is loaded more heavily than the lower half, resulting in a region of larger wake deficit in the upper half.

Now, at $\beta = 10°$, the opposite is expected as the wake undergoes a large lateral expansion and a large vertical contraction in both rotors. This is reflected in the large lateral wake displacement values for both rotors and the low vertical wake displacement. Between the H- and the X-Rotors, the y_c/D of the former is significantly larger than the latter. This is attributed to the two symmetric windward vortices of the H-Rotor that eject the wake laterally rapidly. For the H-Rotor, the wake displacement is asymptotic toward $y_c/D = 0.8$ after $X/L = 8$. This is because, as the wake is ejected laterally, it forms a jellyfish shape beyond $X/L = 7$ due to the movement of the windward vortices. This causes the wake to be displaced vertically and begins to roll-up, which is characterized by z_c/D being increasing after the initial dip at $X/L = 3$. Meanwhile, the X-Rotor shows a nearly linear increase in y_c/D after $X/L = 2$, as the windward vortices are asymmetric and the roll-up of the wake is not achieved even at $X/L = 10$. However, as the wake rolls up close near $X_{w,t}$, there is an increase in z_c/D from around 0.25 to 0.33 between $X/L = 3$ and 10.

From these results, it is difficult to understand which rotor or configuration is more favorable as seen with the $\beta = 0°$ cases, even when the wake appears to have not advected, the wake displacement values are positive and significant. Therefore, understanding the capabilities of each configuration is still limited by this approach but offers valuable quantitative insight into the wake steering capabilities of a VAWT with blade pitch offsets. We can address the limitation of this approach by pairing these results with other supportive quantification methods.

D. Available power (AP)

To further characterize the wake through quantitative approaches, the AP estimation is a widely used method[11,30,60,61] to understand the available power in the wind for a hypothetical identical wind turbine located downstream of the turbine producing the wake. The normalized available power at a specific point in the domain (x_0, y_0, z_0) can be calculated by using

$$C_{AP}(x_0, y_0, z_0) = \frac{1}{A}\int\int_S \frac{\overline{u}^3(x_0, y, z)}{U_\infty^3}\, dz\, dy, \tag{3}$$

where C_{AP} represents the coefficient of available power $(\overline{u}^3/U^3)$ and (x_0, y_0, z_0) is the location of the middle of the hypothetical downstream turbines (HDT), U_∞ is the freestream velocity, $\overline{u}$ is the time-averaged velocity, and A is the frontal area of the rotor. The integration surface S is the region encompassed by the frontal area of the turbine. For the H-Rotor, it is a rectangle, while for the X-Rotor, it is two trapezoids placed one above the other, as the HDT is assumed to be the same dimension as the turbine producing the wake. In this study, we obtain the AP for a HDT that is both inline and at an offset up to 1 D laterally either side from the center of the turbine. This is similar to the moving window method that is employed by Huang, Sciacchitano, and Ferreira,[30] and a schematic of the moving window for the integration is shown in Fig. 8 where the HDT is offset by a distance y_o from the rotor.

The coefficient of available power C_{AP} for an HDT at inline with the rotor is listed in Table III for both the turbines at all pitch offset conditions. As expected, there is an increase in inline AP for the both the rotors with fixed blade pitch offsets than without, due to the lateral and vertical advection of the wake. The $\beta = 10°$ case shows the higher inline AP up to $X/L = 7$ for the X-Rotor, and for the H-Rotor, the $\beta = -10°$ shows the higher inline throughout the domain. For the X-Rotor, this primarily occurs with the increase in advection offered from the pitch case; as the wake curls up around the windward tip-vortex, it is relatively easier for the wake in the upper half of the rotor to go out of the rotor area. As established earlier, the upper half of the X-Rotor produces more loads, which results in higher local velocity deficits. Therefore, pushing this region out of the rotor area proves advantageous for the X-Rotor. For the H-Rotor, when the wake is ejected laterally, it is stretched between the windward and leeward vortices—distributing some part of the wake inside the frontal area of the rotor, which is not observed in the $\beta = -10°$ case. The inline AP becomes comparable to that of the positive pitch around $X/L = 9$ as the wake reenters the frontal area of the turbine in this region observed in Fig. 6. Between the two rotors, the X-Rotor yields more inline AP with both pitch cases to the corresponding H-Rotor pitch cases.

Figure 9 provides insights on the wake advection affecting the AP of an HDT displaced laterally by y_o/D. The results show clear trends that the H-Rotor at $\beta = 10°$ ejects the wake out the most, as the minimum AP is displaced from the center of the rotor rapidly, compared to the other configurations. Consequently, this also indicates that in a hypothetical windfarm, any rotor placed with an offset would be at a disadvantage as it faces large power deficits that it would not have done with the other two pitch cases. The same applies to the X-Rotor as well, albeit to a lesser extent than the H-Rotor.

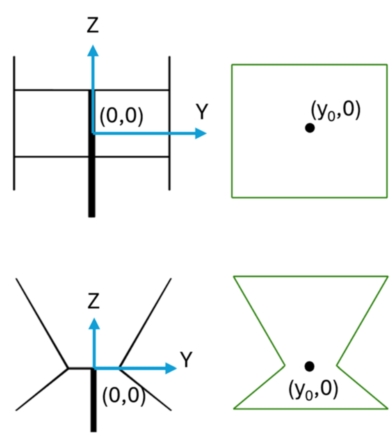

FIG. 8. A schematic of the moving integration window for both the H-Rotor (top) and X-Rotor (bottom) to evaluate the AP. Both the rotors are positioned at origin (0,0). The green contour represents the integration window corresponding to each rotor's frontal area. y_o is the distance by which the HDT is offset from the turbine producing the wake.

TABLE III. The coefficient of available power C_{AP} for a HDT located inline to the rotor producing the wake at pitch offsets of $\beta = -10^\circ, 0^\circ, 10^\circ$ for both the rotors at downstream locations of $X/L = 1$ to 10. The values in the parantheses indicate the gain in C_{AP} as a multiple of the $\beta = 0^\circ$ for the corresponding rotor.

	H-Rotor			X-Rotor		
Pitch β	-10°	0°	10°	-10°	0°	10°
X/L = 1	0.42 (1.20×)	0.35	0.40 (1.15×)	0.44 (1.43×)	0.31	0.42 (1.38×)
X/L = 3	0.56 (1.87×)	0.30	0.53 (1.77×)	0.55 (1.85×)	0.30	0.63 (2.11×)
X/L = 5	0.74 (2.31×)	0.32	0.68 (2.10×)	0.69 (1.91×)	0.36	0.75 (2.07×)
X/L = 7	0.82 (2.32×)	0.36	0.76 (2.15×)	0.81 (1.91×)	0.42	0.82 (1.94×)
X/L = 9	0.83 (2.10×)	0.39	0.81 (2.06×)	0.88 (1.86×)	0.47	0.86 (1.82×)

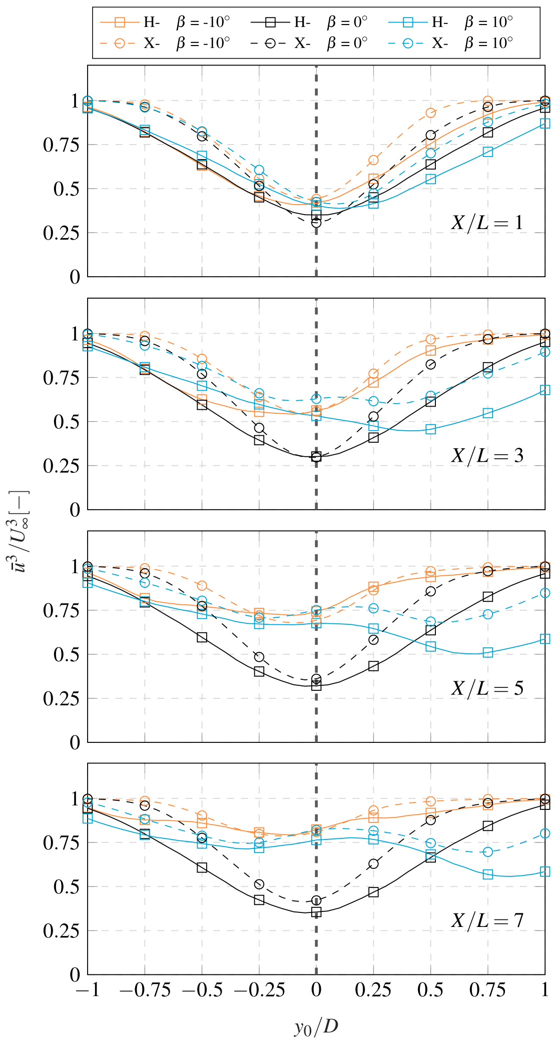

FIG. 9. The coefficient of the available power C_{AP} for an HDT with a lateral displacement y_o/D at downstream locations $X/D = 1$, 3, 5, and 7 for all the pitch cases $\beta = -10^\circ$, 0°, and 10°. Windward is considered as positive y_o/D. The gray dashed line at $y_0/D = 0$ highlights the results of an HDT that is inline with the original rotor. Solid lines with the square markers represent the HDT for an H-Rotor, and the dashed lines with circle markers show results for an HDT for an X-Rotor. Black lines refer to $\beta = 0^\circ$, while orange and cyan represent the $\beta = -10^\circ$ and $\beta = 10^\circ$ cases, respectively.

The $\beta = -10^\circ$, on the other hand, shows good promise in this regard. Not only does it yield higher AP directly inline but it also consistently yields higher AP in the full range of y_o. The vortices ejecting the wake vertically do not hinder the lateral positioning of HDTs as the wake would not be able to physically interact with them. Moreover, the loss in AP in the leeward direction is minimized, allowing the possibility of placing turbines closer to each other in a wind farm setting. This is especially true for the X-Rotor, as the AP on the windward and leeward side shows no large drops. We observe that other than at $X/L = 1$, the minimum AP point for the H-Rotor in this pitch offset still remains close to the inline position, and further downstream it behaves very similarly to that of the X-Rotor while offering higher inline AP. At locations beyond $X/L = 5$, we can observe the continued wake recovery of the X-Rotor due to the higher turbulence compared to the H-Rotor.

Currently, this work neglects the ground effect and does not consider the wake of any turbines adjacent to the one simulated here. The ground effect induces asymmetry in the vertical direction, which impacts the bottom tip-vortex interaction—as the vortices would now tend to move away from each other much faster closer to the ground than away from it. This could affect the wake recovery as the H-Rotor, which relies on the symmetric nature of the vortices would no longer experience it, possibly curtailing the lateral advection rates. However, we are unable to further comment on this as it is beyond the scope of the present study. The wake deflected by adjacent turbines would also be a valuable addition to shed light on the wake control methods in a farm setting. As these are outside the scope of this paper, future studies on this would be instrumental to understand the true capabilities of the wake recovery capabilities of these rotors.

E. Streamwise momentum recovery rates

To understand the wake recovery process, it is important to observe how the momentum is being transported. In this section, the Reynolds Averaged Navier–Stokes (RANS) equation is rearranged to balance the streamwise momentum transport by all the other terms. Moreover, following the approach of Bachant and Wosnik,[62] Boudreau and Dumas,[63] and Huang, Sciacchitano, and Ferreira,[30] the equation is divided by the streamwise velocity component $\bar{u}$. Therefore, the left hand side of the resulting equation (Sec. IV) corresponds to the streamwise component of the streamwise velocity gradient. This is referred to as the streamwise wake recovery rate. The terms on the right hand side indicate the transport of momentum by the lateral and vertical components of the mean velocity fields. The next terms involve the contribution of the mean streamwise pressure gradient as well as the turbulent transport terms in the streamwise, lateral, and vertical directions. The viscous transport contribution has been neglected due to the sufficiently high Reynolds number (chord based $Re = 1.5 \times 10^7$) as well as the lack of a shear layer in this study, as demonstrated by Bachant and Wosnik[62]

$$\frac{\partial \overline{u}}{\partial x} = \frac{1}{\overline{u}}\left[-\overline{v}\frac{\partial \overline{u}}{\partial y} - \overline{w}\frac{\partial \overline{u}}{\partial z} - \frac{1}{\rho}\frac{\partial \overline{p}}{\partial x} - \frac{\partial \overline{u'u'}}{\partial x} - \frac{\partial \overline{u'v'}}{\partial y} - \frac{\partial \overline{u'w'}}{\partial z}\right]. \quad (4)$$

As we use the URANS $k-\varepsilon$ turbulence closure model, instead of using the Reynolds shear stress terms ($-\frac{\partial \overline{u_i' u_j'}}{\partial x_j}$) to calculate the turbulence transport contribution, we use

$$\text{Turbulence transport} = \nu_T \nabla^2 \vec{U}, \quad (5)$$

where ν_T is the turbulent eddy viscosity and $\vec{U}$ is the velocity vector field. This follows the approach employed by Bachant and Wosnik,[24] where they compared the 2D and Three-dimensional (3D) RANS models against water-channel experiments of VAWTs. Furthermore, in these works, the terms are normalized by D/U_∞, as they quantify the mean momentum recovery rate. In this study, as the wake deflects quite significantly with the blade pitch offsets, we instead integrate each transport term inside the area of the wake (99% U_∞). The wake area is considered as it offers insights into the contribution of each term even with severe wake deformation. Therefore, all the results are normalized instead by $1/(DU_\infty)$. Additionally, in this study, we do not focus on the streamwise transport due to pressure. This is because our interest is to understand the contribution of the advective and turbulent transports due to the pitch offsets. Figure 10 shows the wake-integrated streamwise momentum recovery terms for the H- and the X-Rotors at $X/L = 1$ to 10 for all $\beta = [-10°, 0°, 10°]$.

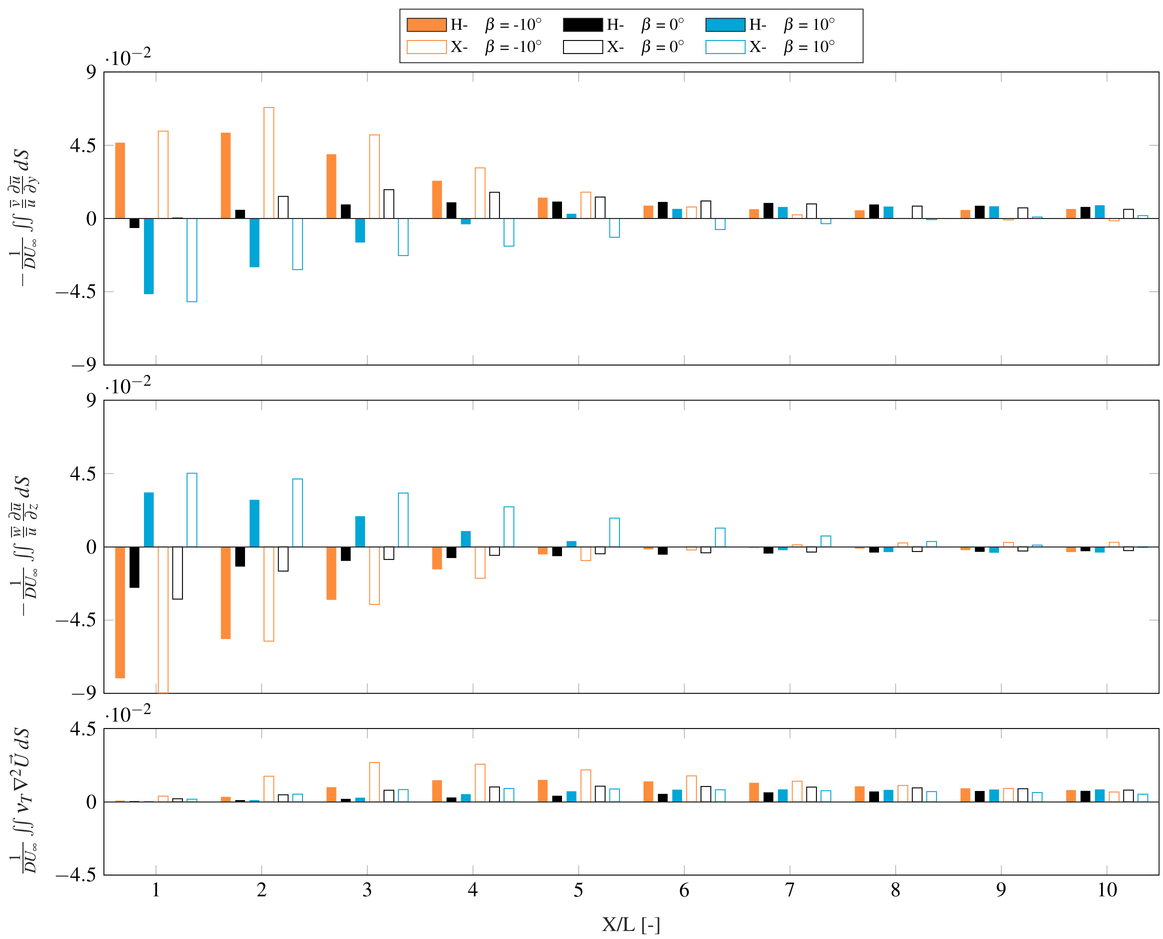

FIG. 10. The streamwise momentum recovery/transport terms integrated in the wake region (S) for the H- and the X-Rotors at $X/L = 1$–10 for all $\beta = [-10°, 0°, 10°]$. The plot shows the integrated lateral momentum transport $\left(-\frac{\overline{v}}{\overline{u}}\frac{\partial \overline{u}}{\partial y}\right)$, vertical momentum transport $\left(-\frac{\overline{w}}{\overline{u}}\frac{\partial \overline{u}}{\partial z}\right)$, and the turbulent transport terms $\frac{1}{DU_\infty}\nu_T\nabla^2\vec{U}$, from top to bottom tiles, respectively. All quantities are normalized by $\frac{1}{DU_\infty}$ after integration. The solid bars represents the H-Rotor momentum terms, while the outlined bars represents the X-Rotor terms. The orange, black, and cyan bars indicate the pitch cases $\beta = [-10°, 0°, 10°]$, respectively. All plots are scaled to be in the same range, with crops applied at the third tile to reduce space.

We can see that in general, the advective transport terms are much larger than the turbulent terms in the near wake for all cases. As we move downstream, the advective transport decreases rapidly and the turbulent transport increases to become comparable (around $X/L = 5$), before it gradually reduces again (after $X/L = 8$). This explains the velocity contours observed in Fig. 6, where the velocity deficit for $\beta = 0^\circ$ decreases after $X/L = 3$, as the turbulence mixes in a high momentum flow with the wake. Moreover, in all pitch cases, the turbulent transport contribution of the X-Rotor is higher than that of the H-Rotor. This is effectively due to the lower local velocity deficit present in the X-Rotor, which gives rise to high-energy turbulent eddies earlier when compared to H-Rotor. This is demonstrated in Fig. 16 in Appendix C.

The rest of the discussion will correlate the observations from Fig. 6 to understand the momentum transport quantification while also shedding light on the wake characteristics. For the $\beta = 0^\circ$ case, both the rotors show higher contribution from the vertical transport terms until $X/L = 2$ as the vertical expansion of the wake replaces high momentum of the freestream with the low momentum of the wake (outside the rotor area). Beyond this, the freestream is transported more in the lateral direction, which is reflected by the higher lateral transport, before turbulence transport competes with it in the far wake region. Interestingly, the X-Rotor shows higher rates of momentum recovery in the lateral direction between $X/L = 2$ and 7, while showing higher vertical momentum recovery rates between $X/L = 1$ and 3. This explains the velocity profile of the X-Rotor, as the wake is mostly concentrated inside the frontal area of the rotor, with mostly freestream immediately outside the rotor area. This contrasts the wake of the H-Rotor as we observed a bigger spread of the wake from the rotor area.

At $\beta = -10^\circ$, the lateral and vertical contributions of the momentum recovery are magnified for both the rotors when compared to the baseline case. In this case, the vertical transport overshadows the lateral transport terms at $X/L = 1$ as the wake is ejected vertically for both the rotors. However, the lateral terms become dominant from $X/L = 3$. This is explained by the rapid influx of a high momentum flow into the frontal area of the rotors observed in the velocity contours between $X/L = 3$ and 5, beyond which turbulent dissipation occurs. The X-Rotor shows higher momentum recovery rates than the X-Rotor in both directions due to its higher vorticity strengths. Interestingly, at $X/L = 8$ and beyond, the vertical advection contribution in the H-Rotor increases slightly. This is due to the wake gradually reentering the frontal area of the rotor. However, this value is insignificant compared to the lateral and the turbulent recovery rates, indicating that the momentum is increasing in these regions. Furthermore, the wake is mostly outside of the rotor area for the H- and the X-Rotors from $X/L = 5$, which indicates that any quantification of the recovery rates will be pertained to the wakes themselves and not correlated with the inline AP.

At $\beta = 10^\circ$, both the lateral and vertical momentum recovery rates of both rotors are still significantly larger than the baseline case and remain dominant until the turbulence transport increases further downstream. The lateral transport is significantly negative as it replaces a high momentum flow outside the rotor area with a low momentum flow, while the vertical transport term does the opposite. For both the rotors, the lateral transport contributes slightly more than the vertical transport term until around $X/L = 3$, where the vertical transport contributes more toward momentum recovery. This explains the significant increase in freestream entering the rotor area from the top and bottom in both rotors. Notably, the both the advective transport in the X-Rotor remains relevant until $X/L = 7$, beyond which the turbulence becomes dominant. Another distinct observation for the H-Rotor is that the advective transport terms flip much earlier than for the X-Rotor. This is because the H-Rotor pushes the wake much farther laterally than the X-Rotor by $X/L = 5$—which causes a pocket of high momentum to exist between the rotor frontal area and the low momentum wake that is displaced by a significant amount (this is also quantified in Fig. 7). As we move downstream, the wake is further moved from the rotor area, which increases the size of this high momentum pocket, consequently increasing the contribution to momentum recovery. This occurs further downstream for the X-Rotor due to the lower wake lateral displacement of this configuration. The same phenomenon explains the flip in the vertical recovery rates as well.

F. Mean kinetic energy flux

Understanding the flux of mean kinetic energy (KE) gives insight into the power replenishment of wind farms. In this case, we primarily focus this study on the power replenishment of the mean kinetic energy for isolated H- and X-Rotors. This approach is also used before by Cortina *et al.*[64] to study an isolated wind turbine and by Hezaveh and BouZeid[65] to study the same in a wind farm. In this work, we follow the approach used by the former than the latter. The mean KE of the flow is represented as $K = \frac{1}{2}(\overline{u^2} + \overline{v^2} + \overline{w^2})$, where $\overline{u}$, $\overline{v}$, and $\overline{w}$ are the time-averaged streamwise, lateral, and vertical components of the velocity field, respectively. Therefore, the flux of the mean kinetic energy Q_V through a closed control volume V behind these VAWTs can be obtained through

$$Q_V = \iiint_V \overline{u_i} \frac{\partial K}{\partial x_i} dV. \tag{6}$$

The work by Cortina *et al.*[64] shows the use of divergence theorem to convert the volume integral to surface integrals for this term, which reduces Eq. (6) to the surface integral of the mean KE flux as

$$Q_S = \iint_S (\overline{u_i} K)\hat{n}_i dS. \tag{7}$$

The flux of the mean kinetic energy also has other components from the energy equation, such as the turbulent KE production, viscous dissipation, and the pressure flux terms. As our interest primarily lies in the lateral and vertical advective fluxes due to the blade pitch angles, this analysis will not constitute these terms as well as the advective flux in the streamwise direction. Figure 11 shows a representation of the control surfaces considered in this study, along which the fluxes are evaluated. In this study, we consider that fluxes entering the surface and going into the encompassed control volume are positive, and vice versa. Now, as the tangential components of velocity corresponding to each surface would not contribute to the flux, simplifications can be made to the flux terms as mentioned in detail in Cortina *et al.*[64]

The advective mean kinetic energy flux through the surfaces S_1, S_2, S_3, and S_4, integrated along the transverse length of the surface, is shown in Fig. 12.

As expected, we observe that the fluxes through these surfaces are much larger for the pitched cases than for the baseline case. For the

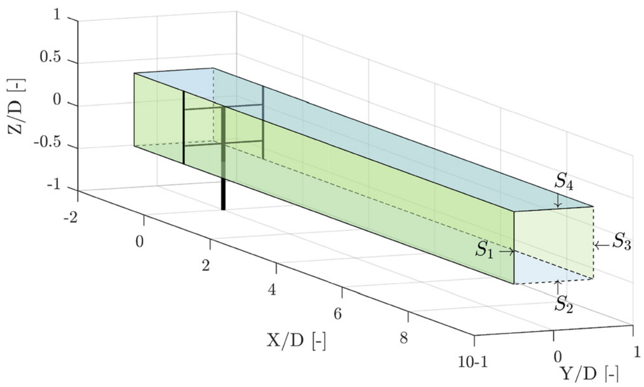

FIG. 11. Schematic of the control surfaces (S_1, S_2, S_3, S_4) along which the mean KE flux in the flow is evaluated. S_1 and S_3 pass through the upper and lower tips of the rotors on the leeward and windward sides, respectively. Meanwhile, S_2 and S_4 pass through the lower blade tips and the upper blade tips, respectively. The fluxes entering the surfaces are considered positive.

baseline case, the mean KE flux is very low, if not null, save for the exception of S_3, where the freestream is brought into the control volume due to the vertical expansion of the wake. Additionally, in S_3, the X-Rotor reports marginally higher flux than the H-Rotor due to the stronger vortices.

At $\beta = -10°$, the kinetic energy flux is low at S_1 compared to the other surfaces. This is because the induced velocity by the leeward vortices is balanced by the windward vortices at this location. This is also visibly noticeable in the velocity contours (Fig. 6) where the wake loiters around the region of the S_1 surface. However, beyond $X/L = 5$, the H-Rotor shows negative flux, indicating the wake exiting S_1. This continues to increase in magnitude as the windward vortices move toward the leeward side. At surface S_3, we see a large positive flux for both rotors inside the rotor region. This occurs as a result of the freestream entering this surface for both rotors as the wake is pushed out vertically. However, this flux decreases sharply after for the X-Rotor, while this decrease is instead gradual for the H-Rotor. This is because, in the X-Rotor, the root vortex merges with the vortices in the upper tip, eventually propelling the upper vortices vertically out of the rotor area. This happens at a much lower extent in the H-Rotor, which gradually continues to bring in high KE flow through this surface. In surfaces S_2 and S_4, the H-Rotor sees the same quantity of flux exiting the surfaces due to its symmetrical geometry. Meanwhile, as expected, the X-Rotor sees a larger flux through S_4 than S_2 due to the much stronger vortex pair at the top than the bottom of the rotor. The X-Rotor also sees a much higher flux magnitudes due to the stronger tip-vortex pairs. However, while the flux magnitude through S_2 gradually reduces downstream, at S_4, it experiences a steeper reduction as the upper tip vortices propel each other further upward, while the bottom vortices do this at a much lower extent, thereby still inducing flux through S_2.

At $\beta = 10°$, we see negative fluxes through S_1 and S_3, while positive fluxes through S_2 and S_4 for both rotors. This is not surprising, considering the advection of velocity in this configuration. In all planes, there is a spike in the flux in the rotor region while gradually tending toward zero, with the notable exception of S_3. At S_3, the spike is followed sharply by a decrease in magnitude at $X/L = 0.2$, which then increases after $X/L = 1.5$ to then decrease again after $X/L = 5$. This odd behavior is because the wake center passing through S_3, which causes a decrease in flux due to the lower mean KE, which then increases again after the windward wake center goes beyond S_3 after $X/L = 5$. This is also reflected in the quantification of wake displacement from Fig. 7. This is more observable in this case than $\beta = -10°$ as the flux is very unequally distributed between S_1 and S_4. The X-Rotor exhibits this closer downstream than the H-Rotor due to the cohesion between the root and tip-vortices, which pushes the wake quickly, and the root vortices dissipate. Again, due to the symmetric geometry of the H-Rotor, the fluxes entering through S_2 and S_4 would be equal, while the X-Rotor shows a marginally higher value through S_4 than S_2.

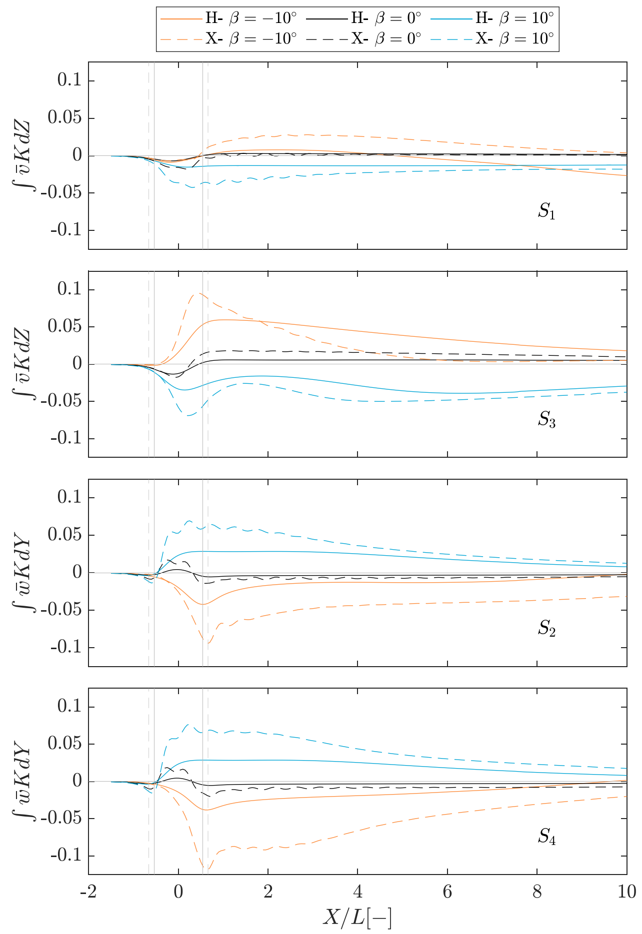

FIG. 12. Line integrated advective flux of the mean KE, integrated along the transverse direction of the control surfaces S_1, S_2, S_3, and S_4, as a function of the streamwise location *X*/*L*, where *L* is the characteristic length scale. The flux terms are normalized by the term $1/U_\infty^3 L_i$, where U_∞ is the freestream velocity and the L_i is the length of the control surface S_i over which the integral is computed. The gray vertical solid and dashed lines indicate the most upwind and downwind locations of the H- and X-Rotors, respectively. The solid gray horizontal line denotes the zero flux of mean kinetic energy.

IV. CONCLUSIONS AND FUTURE WORK

A numerical analysis of the wake recovery capability of VAWTs with a fixed blade pitch as well as its mechanism between two distinct

VAWT geometries, H- and X-, is analyzed in this study. The study contributed the following: (1) provided insight into the parameters that drive the wake recovery mechanism between these rotor geometries and (2) a systematic analysis to qualitatively and quantitatively characterize the wake recovery capability of the H- and the X-Rotors with fixed pitch offsets. The results are generated using the actuator line method (ALM) with *OpenFOAM* through the *turbinesFOAM* library.

The conclusions corresponding to the mechanism of wake recovery between the two rotors are as follows:

- The vortex system of the two rotors is significantly different due to the distinct rotor geometries, and it drastically affects the wake recovery mechanism associated with VAWT pitch offsets. The windward vortices become the dominant driver to advect the wake with blade pitch—for the H-Rotor, the vortices work cohesively to push the wake out of the rotor and bring freestream vertically into the rotor area with the positive pitch case, while pushing the wake up vertically out with the negative pitch case. The X-Rotor, due to the asymmetric geometry, is seen to contribute more to the wake recovery through the upper half than the lower half, due to the higher vortex strengths associated with the upper blade loads than the lower blades. Additionally, the circulation difference at the root of the X-Rotor blades produces a root vortex that affects the overall vortex system in the near wake in both pitch cases. In this study, the root vortex was less dominant compared to the tip-vortices and aided the recovery of the wake in the upper half of the X-Rotor.
- The advection terms in both rotors play a crucial role in the wake recovery process of the rotors. In general, the advection dominates the near wake, while turbulence takes over the recovery process from around $X/L = 5$. However, the magnitude of advection increases significantly with pitch offsets—increasing the recovery process tremendously. In the negative pitch cases, the contribution of turbulence also increases and stays relevant throughout the domain.
- For the X-Rotor, compared to the slower wake recovery while only allowing pitch control for the upper blades (Giri Ajay and Simao Ferreira[37]), the wake deflection is significantly improved in this study. This is due to the twin root vortices formed in the windward side, which work cohesively with the windward vortices to advect the wake. Moreover, the stronger lower blade tip-vortices now actively deflect the wake of the lower half.

The important conclusions that we gained about the quantification of the wake recovery are:

- Overall, pitching the blades to increase lateral and vertical advection proved to result in much higher inline available power (AP) than for rotors without blade pitch offsets. Pitching the blades showed an increase in the inline AP of the H-Rotor by 2.3 times at $X/L = 5$ and by 2.08 times for the X-Rotor. The X-Rotor also showed the highest inline AP in the near wake with the positive pitch configuration. However, after understanding the variation of AP at lateral offsets, it is evident that the H-Rotor at positive pitches decreases the AP laterally due to the lateral advection of the wake, which potentially can reduce the power of an adjacent turbine downstream. However, the negative pitch configuration does not have this significant drawback as the wake is vertically ejected from the rotor area—this increasing inline AP while not significantly compromising the AP in the lateral direction.
- Quantifying the vertical wake center deflection for H-Rotor can be misleading due to the vertical symmetry. Therefore, a slight modification of this approach is employed in this study, which sheds light into the wake displacements with blade pitch offsets. The H-Rotor with the positive blade pitch showed the most lateral wake displacement, while both the rotors showed nearly the same wake displacements with the negative pitch. Overall, understanding the displacement of the wake cannot be used as a stand-alone measure of wake recovery effectiveness and required complementary analyses.
- The mean kinetic flux further emphasized the increase in the mean kinetic energy behind the rotor through the lateral and vertical advection associated with the blade pitching. The X-Rotor showed the highest flux magnitudes in all configurations, as the vortices of the X-Rotor are much larger. Furthermore, as the rotor is asymmetric, the flux through the upper surface is much larger than the lower half for the negative pitch, while relatively equal with the positive pitch offsets.

For future expansions of this work, we recommend a more complete study involving ground effects, atmospheric boundary layers, and the effect of the advected wake of adjacent wind turbines in wind farms to gain crucial insight into the effectiveness of VAWT wake recovery with blade pitch offsets in close to real-world operations.

ACKNOWLEDGMENTS

We wish to acknowledge the support of Dr. Andrea Sanvito, André Ribeiro, and Nirav Dangi on their help with the ALM sensitivity study. We also wish to acknowledge David Bensason on the helpful discussions on the quantification analysis of this paper. We would also like to thank Dr. Delphine de Tavernier on their support and assistance with the review process. We gratefully acknowledge the computational resources provided on the DelftBlue cluster by the Delft High Performance Computing Centre (DHPC)[54] at the Delft University of Technology to perform the required simulations in this study. We also wish to thank the European Union's Horizon 2020 research and innovation programme for funding this research (Grant Agreement No. 101007135) as part of the XROTOR project (https://doi.org/10.3030/101007135).

AUTHOR DECLARATIONS

Conflict of Interest

The authors have no conflicts to disclose.

Author Contributions

Adhyanth Giri Ajay: Conceptualization (equal); Data curation (lead); Formal analysis (lead); Investigation (lead); Methodology (lead); Visualization (lead); Writing – original draft (lead); Writing – review & editing (equal). **Carlos Simao Ferreira:** Conceptualization (equal); Formal analysis (supporting); Funding acquisition (lead); Investigation (supporting); Methodology (supporting); Project administration (lead); Supervision (lead); Validation (supporting); Writing – review & editing (equal).

DATA AVAILABILITY

The data that support the findings of this study are openly available in 4TU. ResearchData repository at https://doi.org/10.4121/13913c03-5173-48a7-8aa1-08305fa52bb0.

APPENDIX A: MODIFICATIONS TO *TURBINESFOAM*

1. Tuning $\varepsilon/\Delta_{grid}$ for optimum blade load representation

To tune the *turbinesFoam* model to give the best representation of the blade loads, we looked at varying the $\varepsilon/\Delta_{grid}$ along with mesh sizes Δ_{grid}. A similar sensitivity study is performed by Sanvito *et al.*[66] for ALM while describing a novel velocity sampling method. Figure 13 shows the variations of normal and tangential forces for the H-Rotor, integrated along the blade span, to $\varepsilon/\Delta_{grid}$. The predicted forces from the free-wake vortex model CACTUS are also presented as a benchmark to attain with ALM. Comparing the normal forces, we understand that the ALM model variations all fall short of the CACTUS model in the upwind half, but a large spread is observed in the downwind half. With increasing $\varepsilon/\Delta_{grid}$, the normal loads tend toward CACTUS plots in the upwind half but overpredict the loads in the downwind half. The tangential force portrays a different story—all the ALM model variations predict larger loads than CACTUS. The difference is exacerbated in the downwind half, where reducing $\varepsilon/\Delta_{grid}$ causes the loads to approach CACTUS loads, while the upwind half does the opposite.

Using these two plots as a reference, $\varepsilon/\Delta_{grid} = 2.5$ at a resolution of D/20 is the value chosen as it is the average of the two extremes. To capture the turbulence, the mesh resolution is doubled to D/40. However, to maintain the same load profiles, the $\varepsilon/\Delta_{grid}$ has to also be doubled, so that the physical value of ε

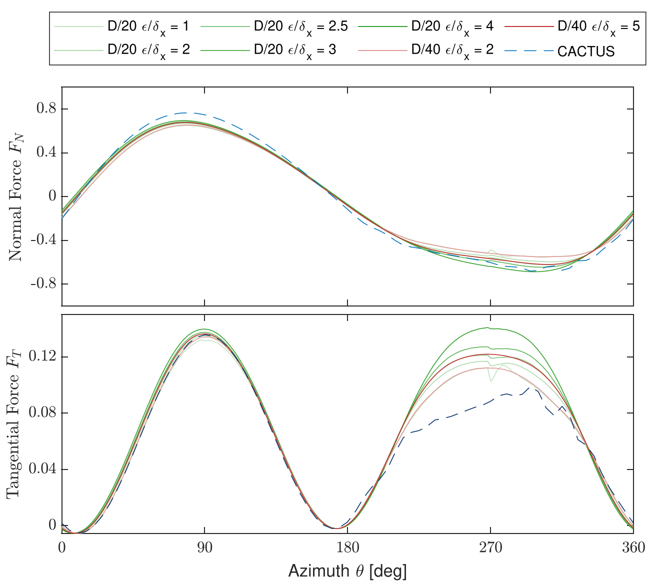

FIG. 13. Normal and tangential force variations of the H-Rotor with ϵ/Δ_{grid} and Δ_{grid}. Increasing opacity indicates increasing ϵ/Δ_{grid}, with the greens associated for the grid resolution of D/20 and the red for D/40. The dashed line indicates blade loads from CACTUS. Loads are normalized by $1/(0.5\rho U^2 A)$.

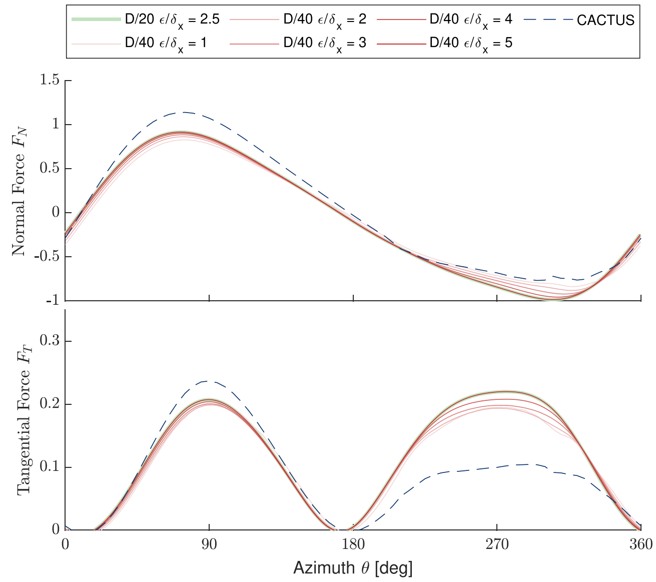

FIG. 14. Normal and tangential force variations of the X-Rotor with ϵ/Δ_{grid} and Δ_{grid}. Increasing opacity indicates increasing ϵ/Δ_{grid}, with the green associated for the grid resolution of D/20 and the red for D/40. The dashed line indicates blade loads from CACTUS. Loads are normalized by $1/(0.5\rho U^2 A)$.

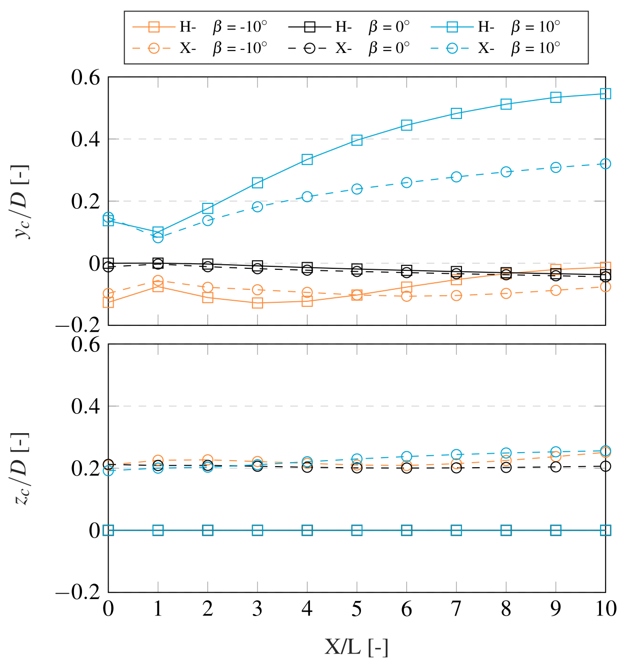

FIG. 15. The wake center displacement in the lateral (y_c/D) and axial (z_c/D) displacements. Solid lines with squares represent the H-Rotor, and dashed lines with circles represent the X-Rotor. Orange, black, and cyan indicate pitch offsets of $\beta = [-10^\circ, 0^\circ, 10^\circ]$, respectively.

remains the same. This is seen in the red lines, where $\varepsilon/\Delta_{grid} = 5$ at D/40 matches very well with the $\varepsilon/\Delta_{grid} = 2.5$ at D/20. Therefore, the chosen configuration was a rotor mesh resolution of D/40, with $\varepsilon/\Delta_{grid} = 5$, which corroborates the results of Sanvito *et al.*[66]

The X-Rotor has a different diameter D as well as chord c, which requires the sensitivity study to be repeated again. However, we set the mesh resolution to be the constraint, as we want to minimize variations between the two rotor simulation setups. Therefore, Fig. 14 shows the variations of normal and tangential forces for the X-Rotor, integrated along the blade span, to $\varepsilon/\Delta_{grid}$. Here, we can observe that the increase in $\varepsilon/\Delta_{grid}$ leads to an increase in magnitudes of the loads. However, the loads in the upwind half are always underpredicted, while the loads in the downwind half are overpredicted—regardless of the $\varepsilon/\Delta_{grid}$ value. Furthermore, the tangential loads show similar pattern to the H-Rotor—increasing $\varepsilon/\Delta_{grid}$ brings the forces closer to CACTUS in the upwind half, but cause them to be overpredicted by a large amount in the downwind half. The difference in tangential forces is significant, and there is no obvious choice of $\varepsilon/\Delta_{grid}$ to be used in the study. We chose $\varepsilon/\Delta_{grid} = 2$ at D/40 for the X-Rotor as this offers good balance in normal loads in the upwind and downwind halves, while not straying too far away from the tangential forces in the upwind half. The tangential forces would mostly affect the torque and the power performance, as the normal loads are not included.

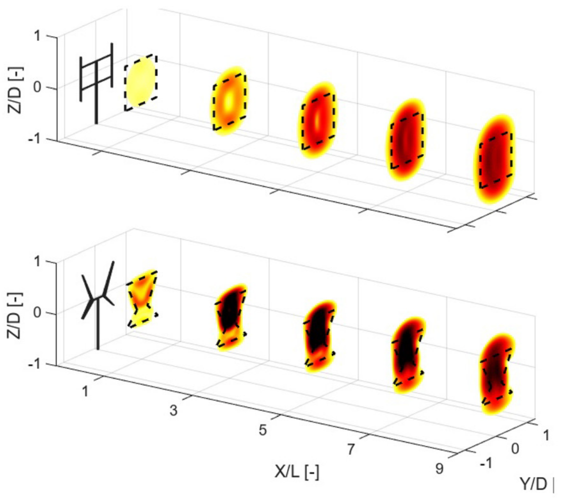

(a) $\beta = 0°$ (baseline)

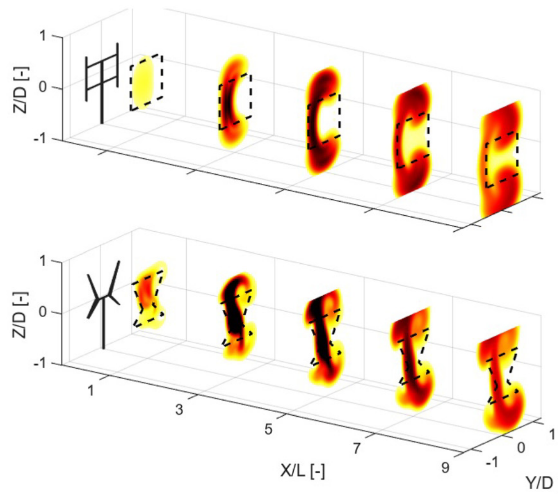
(b) $\beta = -10°$

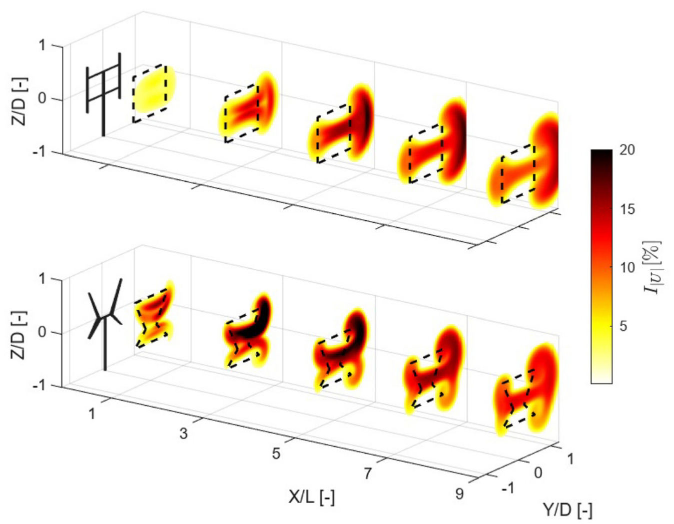
(c) $\beta = 10°$

FIG. 16. Turbulence intensity of the H- and the X-Rotors at $\beta = -10°, 0°, 10°$, respectively, at downstream locations $X/L = 1$ to 10, where L is the characteristic streamwise length scale. The black dashed lines indicate the projected frontal area of the rotor on the corresponding plane. The low turbulence intensities (less than 2%) were removed to enhance the visibility of the isometric plots.

Regardless, as the wake of the turbines is characterized by the thrust, the normal load is of primary significance, and the results show variation from CACTUS, which we consider acceptable for this study.

2. Inclusion of cone angle

turbinesFoam, in its current published stage, does not accept inputs for the cone angle for rotor blades. Therefore, the model would not allow for the analysis of VAWTs with non-vertical span such as the DeepWind VAWT concept,[67] or in this case, the X-Rotor VAWT concept.[33] This leads to a false representation of the blade forces in the fluid domain, especially for the X-Rotor with two sets of coned blades. So, the input parameters were modified to include a cone angle option. The modification is done after Line 132 in *turbinesFoam/src/fvOptions/crossFlowTurbineALSource/crossFlowTurbineALSource.C/createBlades()* and is shown below.

Here, the variable "cone" is the additional input parameter that governs the cone angle of the blade from the vertical axis. Consequently, the input file is modified to include the "cone" input. As the forces from the blade use the "spanDir" parameter to determine the direction of force, the initial vertical and the radial components of the span direction are altered based on the cone angle. The cone angle follows the convention that the clock-wise angle from the vertical is positive and vice versa. The modified source code is available on GitHub (Giri Ajay and Simao Ferreira[46]), which houses several branches with the different $\varepsilon/\Delta_{grid}$ values used to analyze the loads and the velocity fields of the rotor.

APPENDIX B: WAKE CENTER DEFLECTION

In this instance, we use the conventional approach of the "center of mass" to evaluate the wake center deflection. The wake center deflection is evaluated by

$$y_c(X) = \frac{\int\int y\,\Delta U(x,y,z)\,dy\,dz}{\int\int \Delta U(x,y,z)\,dy\,dz}, \quad \text{and} \quad z_c(X) = \frac{\int\int z\,\Delta U(x,y,z)\,dy\,dz}{\int\int \Delta U(x,y,z)\,dy\,dz}. \tag{B1}$$

Fig. 15 shows the wake center deflection for both the rotors at pitch cases $\beta = -10^\circ, 0^\circ, 10^\circ$. We can notice that the lateral deflection is quite evident and is captured well. This reflects that the $\beta = 10^\circ$ shows the highest lateral wake deflection due to the strong windward vortices advecting the wake out laterally. However, we see that the vertical wake center deflection is not captured at all for the H-Rotor. This is due to its symmetric geometry, where the wake is equally expanded/contracted in the vertical direction. The X-Rotor shows some difference, but that is mainly attributed to the difference in the upper and lower blade loads, which cause the values here to be higher. However, not much information can be drawn from this analyses as the vertical deflection of the H-Rotor is missing completely. This makes the results very misleading and leads to non-intuitive results.

APPENDIX C: TURBULENCE INTENSITY

The turbulence intensity TI (in %) is showcased in Fig. 16 for the H- and the X-Rotors at $\beta = -10^\circ, 0^\circ, 10^\circ$.

REFERENCES

[1] A. Evans, V. Strezov, and T. J. Evans, "Assessment of sustainability indicators for renewable energy technologies," Renewable Sustainable Energy Rev. **13**, 1082–1088 (2009).
[2] T. F. Ishugah, Y. Li, R. Z. Wang, and J. K. Kiplagat, "Advances in wind energy resource exploitation in urban environment: A review," Renewable Sustainable Energy Rev. **37**, 613–626 (2014).
[3] W. Tjiu, T. Marnoto, S. Mat, M. H. Ruslan, and K. Sopian, "Darrieus vertical axis wind turbine for power generation II: Challenges in HAWT and the opportunity of multi-megawatt Darrieus VAWT development," Renewable Energy **75**, 560–571 (2015).
[4] H. Lee, S. K. Poguluri, and Y. H. Bae, "Development and verification of a dynamic analysis model for floating offshore contra-rotating vertical-axis wind turbine," Energy **240**, 122492 (2022).
[5] P. Flaszyński, F. Wasilczuk, M. Piotrowicz, J. Telega, K. Mitraszewski, and K. S. Hansen, "Numerical simulations for a parametric study of blockage effect on offshore wind farms," Wind Energy **27**, 53–74 (2024).
[6] M. Bastankhah and F. Porté-Agel, "Wind farm power optimization via yaw angle control: A wind tunnel study," J. Renewable Sustainable Energy **11**, 23301 (2019).
[7] M. Bastankhah and F. Porté-Agel, "Experimental and theoretical study of wind turbine wakes in yawed conditions," J. Fluid Mech. **806**, 506–541 (2016).
[8] P. Fleming, M. Churchfield, A. Scholbrock, A. Clifton, S. Schreck, K. Johnson, A. Wright, P. Gebraad, J. Annoni, B. Naughton, J. Berg, T. Herges, J. White, T. Mikkelsen, M. Sjöholm, and N. Angelou, "Detailed field test of yaw-based wake steering," J. Phys. Conf. Ser. **753**, 052003 (2016).
[9] M. F. Howland, J. Bossuyt, L. A. Martínez-Tossas, J. Meyers, and C. Meneveau, "Wake structure in actuator disk models of wind turbines in yaw under uniform inflow conditions," J. Renewable Sustainable Energy **8**, 43301 (2016).
[10] P. Fleming, J. Annoni, J. J. Shah, L. Wang, S. Ananthan, Z. Zhang, K. Hutchings, P. Wang, W. Chen, and L. Chen, "Field test of wake steering at an offshore wind farm," Wind Energy Sci. **2**, 229–239 (2017).
[11] J. Bossuyt, R. Scott, N. Ali, and R. B. Cal, "Quantification of wake shape modulation and deflection for tilt and yaw misaligned wind turbines," J. Fluid Mech. **917**, 1–28 (2021).
[12] C. Cossu, "Evaluation of tilt control for wind-turbine arrays in the atmospheric boundary layer," Wind Energy Sci. **6**, 663–675 (2021).
[13] J. A. Frederik, B. M. Doekemeijer, S. P. Mulders, and J. W. van Wingerden, "The helix approach: Using dynamic individual pitch control to enhance wake mixing in wind farms," Wind Energy **23**, 1739–1751 (2020).
[14] D. V. D. Berg, D. D. Tavernier, and J. W. V. Wingerden, "Using the helix mixing approach on floating offshore wind turbines," J. Phys. Conf. Ser. **2265**, 042011 (2022).
[15] J. O. Dabiri, "Potential order-of-magnitude enhancement of wind farm power density via counter-rotating vertical-axis wind turbine arrays," J. Renewable Sustainable Energy **3**, 043104 (2011).
[16] M. Kinzel, Q. Mulligan, and J. O. Dabiri, "Energy exchange in an array of vertical-axis wind turbines," J. Turbul. **13**, N38 (2012).
[17] S. Zanforlin and T. Nishino, "Fluid dynamic mechanisms of enhanced power generation by closely spaced vertical axis wind turbines," Renewable Energy **99**, 1213–1226 (2016).
[18] J. Meyers and C. Meneveau, "Large eddy simulations of large wind-turbine arrays in the atmospheric boundary layer," AIAA Paper No. 2010-827, 2010.
[19] S. Shamsoddin and F. Porté-Agel, "Large eddy simulation of vertical axis wind turbine wakes," Energies **7**, 890–912 (2014).
[20] V. Mendoza, P. Bachant, C. Ferreira, and A. Goude, "Near-wake flow simulation of a vertical axis turbine using an actuator line model," Wind Energy **22**, 171–188 (2019).
[21] M. Kinzel, D. B. Araya, and J. O. Dabiri, "Turbulence in vertical axis wind turbine canopies," Phys. Fluids **27**, 115102 (2015).
[22] V. Rolin and F. Porté-Agel, "Wind-tunnel study of the wake behind a vertical axis wind turbine in a boundary layer flow using stereoscopic particle image velocimetry," J. Phys. Conf. Ser. **625**, 012012 (2015).
[23] P. Chatelain, M. Duponcheel, S. Zeoli, S. Buffin, D. G. Caprace, G. Winckelmans, and L. Bricteux, "Investigation of the effect of inflow turbulence on vertical axis wind turbine wakes," J. Phys. Conf. Ser. **854**, 012011 (2017).

[24]P. Bachant and M. Wosnik, "Modeling the near-wake of a vertical-axis cross-flow turbine with 2-D and 3-D RANS," J. Renewable Sustainable Energy **8**, 53311 (2016).
[25]P. Ouro, S. Runge, Q. Luo, and T. Stoesser, "Three-dimensionality of the wake recovery behind a vertical axis turbine," Renewable Energy **133**, 1066–1077 (2019).
[26]C. S. Ferreira, "The near wake of the VAWT 2D and 3D views of the VAWT aerodynamics," Ph.D. thesis (Delft University of Technology, 2009).
[27]B. LeBlanc and C. Ferreira, "Estimation of blade loads for a variable pitch vertical axis wind turbine with strain gage measurements," Wind Energy **25**, 1030–1045 (2022).
[28]B. LeBlanc and C. Ferreira, "Estimation of blade loads for a variable pitch vertical axis wind turbine from particle image velocimetry," Wind Energy **25**, 313–332 (2022).
[29]A. Jadeja, "Wake deflection technique for vertical axis wind turbines using actuator line model in OpenFOAM," Master's thesis (Delft University of Technology, 2018).
[30]M. Huang, A. Sciacchitano, and C. Ferreira, "On the wake deflection of vertical axis wind turbines by pitched blades," Wind Energy **26**, 365 (2023).
[31]M. Huang, Y. V. Patil, A. Sciacchitano, and C. Ferreira, "Experimental study of the wake interaction between two vertical axis wind turbines," Wind Energy **26**, 1188–1211 (2023).
[32]M. Huang, "Wake and wind farm aerodynamics of vertical axis wind turbines," Ph.D. thesis (Delft University of Technology, 2023).
[33]W. Leithead, A. Camciuc, A. K. Amiri, and J. Carroll, "The X-rotor offshore wind turbine concept," J. Phys. Conf. Ser. **1356**, 012031 (2019).
[34]D. Bensason, A. Sciacchitano, and C. Ferreira, "Near wake of the X-rotor vertical-axis wind turbine," J. Phys. Conf. Ser. **2505**, 012040 (2023).
[35]A. Giri Ajay, L. Morgan, Y. Wu, D. Bretos, A. Cascales, O. Pires, and C. Ferreira, "Aerodynamic model comparison for an x-shaped vertical-axis wind turbine," Wind Energy Sci. **9**, 453–470 (2024).
[36]D. Bensason, A. Sciacchitano, A. Giri Ajay, and C. S. Ferreira, "A study of the near wake deformation of the X-rotor vertical-axis wind turbine with pitched blades," Wind Energy **27**, 1388 (2024).
[37]A. Giri Ajay and C. Simao Ferreira, "Numerical study on wake recovery of vertical-axis wind turbines through fixed blade pitch offsets: H vs x rotors," J. Phys. Conf. Ser. **2767**, 072010 (2024).
[38]J. N. Sørensen and W. Z. Shen, "Numerical modeling of wind turbine wakes," J. Fluids Eng., Trans. ASME **124**, 393–399 (2002).
[39]P. Bachant, A. Goude, and M. Wosnik, "Actuator line modeling of vertical-axis turbines," arXiv:1605.01449 (2016).
[40]H. G. Weller, G. Tabor, H. Jasak, and C. Fureby, "A tensorial approach to computational continuum mechanics using object-oriented techniques," Comput. Phys. **12**, 620–631 (1998).
[41]N. Troldborg, "Acutator line modeling of wind turbine wakes," Ph.D. thesis (Technical University of Denmark, 2009).
[42]L. A. Martínez, S. Leonardi, M. J. Churchfield, and P. J. Moriarty, "A comparison of actuator disk and actuator line wind turbine models and best practices for their use," AIAA Paper No. 2012-0900, 2012.
[43]P. K. Jha, M. J. Churchfield, P. J. Moriarty, and S. Schmitz, "Accuracy of state-of-the-art actuator-line modeling for wind turbine wakes," AIAA Paper No. 2013-0608, 2013.
[44]P. K. Jha, M. J. Churchfield, P. J. Moriarty, and S. Schmitz, "Guidelines for volume force distributions within actuator line modeling of wind turbines on large-eddy simulation-type grids," J. Sol. Energy Eng., Trans. ASME **136**, 031003 (2014).
[45]J. Murray and M. Barone, "The development of CACTUS, a wind and marine turbine performance simulation code," AIAA Paper No. 2011-147, 2011.
[46]A. Giri Ajay and C. S. Ferreira (2024), "A modified version of turbinesFoam that accounts for coned blades," GitHub. https://github.com/Adhyanth29/turbinesFoam_coned_blades.git
[47]W. P. Jones and B. E. Launder, "The prediction of laminarization with a two-equation model of turbulence," Int. J. Heat Mass Transfer **15**, 301–314 (1972).
[48]F. R. Menter, "Two-equation eddy-viscosity turbulence models for engineering applications," AIAA J. **32**, 1598–1605 (1994).
[49]S. McTavish, D. Feszty, and T. Sankar, "Steady and rotating computational fluid dynamics simulations of a novel vertical axis wind turbine for small-scale power generation," Renewable Energy **41**, 171–179 (2012).
[50]A. Rezaeiha, I. Kalkman, and B. Blocken, "CFD simulation of a vertical axis wind turbine operating at a moderate tip speed ratio: Guidelines for minimum domain size and azimuthal increment," Renewable Energy **107**, 373–385 (2017).
[51]M. Wosnik, P. Bachant, V. S. Neary, and A. W. Murphy, "Evaluation of design & analysis code, CACTUS, for predicting cross-flow hydrokinetic turbine performance," Report No. SAND2016-9787 (Sandia National Laboratory, 2016).
[52]P. Meunier and G. R. Spedding, "A loss of memory in stratified momentum wakes," Phys. Fluids **16**, 298–305 (2004).
[53]S. Shamsoddin and F. Porté-Agel, "Effect of aspect ratio on vertical-axis wind turbine wakes," J. Fluid Mech. **889**, R11–R112 (2020).
[54]Delft High Performance Computing Centre (DHPC), see https://www.tudelft.nl/dhpc/ark:/44463/DelftBluePhase1 for "DelftBlue supercomputer (phase 1)" (2022).
[55]Á. Jiménez, A. Crespo, and E. Migoya, "Application of a LES technique to characterize the wake deflection of a wind turbine in yaw," Wind Energy **13**, 559–572 (2010).
[56]P. A. Fleming, P. M. Gebraad, S. Lee, J. W. van Wingerden, K. Johnson, M. Churchfield, J. Michalakes, P. Spalart, and P. Moriarty, "Evaluating techniques for redirecting turbine wakes using SOWFA," Renewable Energy **70**, 211–218 (2014).
[57]S. Guntur, N. Troldborg, and M. Gaunaa, "Application of engineering models to predict wake deflection due to a tilted wind turbine," in *European Wind Energy Conference and Exhibition, EWEC 2012* (European Wind Energy Association, 2012), Vol. 2, pp. 1044–1049.
[58]L. Luo, N. Srivastava, and P. Ramaprabhu, "A study of intensified wake deflection by multiple yawed turbines based on large eddy simulations," in *33rd Wind Energy Symposium* (American Institute of Aeronautics and Astronautics Inc, 2015).
[59]N. J. Wei, I. D. Brownstein, J. L. Cardona, M. F. Howland, and J. O. Dabiri, "Near-wake structure of full-scale vertical-axis wind turbines," J. Fluid Mech. **914**, A17 (2021).
[60]L. Vollmer, G. Steinfeld, D. Heinemann, and M. Kühn, "Estimating the wake deflection downstream of a wind turbine in different atmospheric stabilities: An LES study," Wind Energy Sci. **1**, 129–141 (2016).
[61]H. Zong and F. Porté-Agel, "A point vortex transportation model for yawed wind turbine wakes," J. Fluid Mech. **890**, A8 (2020).
[62]P. Bachant and M. Wosnik, "Characterising the near-wake of a cross-flow turbine," J. Turbul. **16**, 392–410 (2015).
[63]M. Boudreau and G. Dumas, "Comparison of the wake recovery of the axial-flow and cross-flow turbine concepts," J. Wind Eng. Ind. Aerodyn. **165**, 137–152 (2017).
[64]G. Cortina, M. Calaf, and R. B. Cal, "Distribution of mean kinetic energy around an isolated wind turbine and a characteristic wind turbine of a very large wind farm," Phys. Rev. Fluids **1**, 1–18 (2016).
[65]S. H. Hezaveh and E. Bou-Zeid, "Mean kinetic energy replenishment mechanisms in vertical-axis wind turbine farms," Phys. Rev. Fluids **3**, 94606 (2018).
[66]A. G. Sanvito, A. Firpo, P. Schito, V. Dossena, A. Zasso, and G. Persico, "A novel vortex-based velocity sampling method for the actuator-line modeling of floating offshore wind turbines in windmill state," Renewable Energy **231**, 120927 (2024).
[67]L. Vita, U. S. Paulsen, T. F. Pedersen, H. A. Madsen, and F. Rasmussen, "A novel floating offshore wind turbine concept," in *European Wind Energy Conference and Exhibition 2009, EWEC 2009* (European Wind Energy Association, 2009), Vol. 7, pp. 4497–4502.